

Shear Assisted Processing and Extrusion (ShAPE) of Aluminum Alloy 7075, 2024, and Al-12.4TM

Final Technical Report

December 2021

Scott A. Whalen (PI)
Pacific Northwest National Laboratory
902 Battelle Blvd.
Richland, WA 99354
scott.whelen@pnnl.gov
(509) 372-6084

Keerti S. Kappagantula	Timothy Roosendaal
Md. Reza-E-Rabby	Brandon Scott Taysom
Xiao Li	Julian Escobar Atehortua
Nicole R. Overman	Josh Silverstein
Matthew J. Olszta	Nathan Canfield
Tianhao Wang	Daniel Graff
Darrell R. Herling	
Sara Suffield	

Period of Performance: October 2019 – September 2021
CPS 35426 2.1.0.24

DISCLAIMER

This report was prepared as an account of work sponsored by an agency of the United States Government. Neither the United States Government nor any agency thereof, nor Battelle Memorial Institute, nor any of their employees, makes **any warranty, express or implied, or assumes any legal liability or responsibility for the accuracy, completeness, or usefulness of any information, apparatus, product, or process disclosed, or represents that its use would not infringe privately owned rights.** Reference herein to any specific commercial product, process, or service by trade name, trademark, manufacturer, or otherwise does not necessarily constitute or imply its endorsement, recommendation, or favoring by the United States Government or any agency thereof, or Battelle Memorial Institute. The views and opinions of authors expressed herein do not necessarily state or reflect those of the United States Government or any agency thereof.

PACIFIC NORTHWEST NATIONAL LABORATORY
operated by
BATTELLE
for the
UNITED STATES DEPARTMENT OF ENERGY
under Contract DE-AC05-76RL01830

Printed in the United States of America

Available to DOE and DOE contractors from the
Office of Scientific and Technical Information,
P.O. Box 62, Oak Ridge, TN 37831-0062;
ph: (865) 576-8401
fax: (865) 576-5728
email: reports@adonis.osti.gov

Available to the public from the National Technical Information Service
5301 Shawnee Rd., Alexandria, VA 22312
ph: (800) 553-NTIS (6847)
email: orders@ntis.gov <<https://www.ntis.gov/about>>
Online ordering: <http://www.ntis.gov>

Shear Assisted Processing and Extrusion (ShAPE) of Aluminum Alloy 7075, 2024, and Al- 12.4TM

Final Technical Report

December 2021

Scott A. Whalen (PI)
Pacific Northwest National Laboratory
902 Battelle Blvd.
Richland, WA 99354
scott.whelen@pnnl.gov
(509) 372-6084

Keerti S. Kappagantula	Timothy Roosendaal
Md. Reza-E-Rabby	Brandon Scott Taysom
Xiao Li	Julian Escobar Atehortua
Nicole R. Overman	Josh Silverstein
Matthew J. Olszta	Nathan Canfield
Tianhao Wang	Daniel Graff
Darrell R. Herling	
Sara Suffield	

Prepared for
the U.S. Department of Energy
under Contract DE-AC05-76RL01830

Pacific Northwest National Laboratory
Richland, Washington 99354

Executive Summary

The most common aluminum alloys utilized in the aerospace industry are 7075 and 2024 due to their high strength-to-weight ratio compared to advanced high strength steels and other aluminum alloys. Despite excellent performance, these aluminum alloys have seen limited use outside of the aerospace industry due in part to high cost. If high-performance aluminum extrusions could be made more cost effectively by eliminating energy intensive process steps typical of conventional extrusion, then numerous opportunities exist for more widespread adoption. A key reason for the high cost of 7075 and 2024 extrusions (25-75% higher than 6061) is their slow extrusion speed. 7075 and 2024 are limited to 2 m/min and 3.5 m/min respectively in contrast to 6061 which can be extruded at 20–80 m/min. In addition to slow speed, aluminum alloys require numerous thermal treatments throughout the extrusion process including homogenization and pre-heating prior to extrusion, and solution heat treating and artificial aging after extrusion. Each of these steps contribute to the total energy consumed during manufacturing of extruded components. This project investigates the use of ShAPE to improve extrusion speed and reduce, or even eliminate, the typical thermal treatments for high strength aluminum alloys, all while improving material performance.

The overarching goal of this project was to demonstrate that Shear Assisted Processing and Extrusion (ShAPE) can manufacture high-performance aluminum alloy tubing with lower embedded energy and improved mechanical properties compared to conventional extrusion. Unlike conventional extrusion where the billet is rammed against a stationary die using a strictly linear motion, the ShAPE process superimposes a rotational shear force by spinning the die while the billet is plunged. Compared to conventional linear extrusion, the ShAPE process imparts significantly more strain into the feedstock material which enables the formation of novel microstructures. These microstructures manifest an array of property and process improvements for extrusion of high-performance aluminum alloys.

The following accomplishments were achieved for this project:

- Extrusion of 7075 at 12.2 meters/min compared to 2 meters/min for conventional extrusion.
- Elimination of 7075 billet homogenization (430 °C for 20 hours) which is required prior to conventional extrusion.
- Elimination of 7075 billet pre-heating (400 °C for 1 hour) in a separate furnace which is required prior to conventional extrusion.
- Elimination of 7075 post-extrusion solution heat treatment (480 °C for 1 hour) for extrusions made from homogenized billets. The enabled T6 properties with merely a T5 heat treatment.
- Achieved 7075-T6 yield strength = 531 MPa, ultimate tensile strength = 596MPa, and elongation = 17.4% for extrusions made from unhomogenized billets. Exceeds the ASTM and ASM standard, and typical industry values.
- Achieved 7075-T5 yield strength = 535 MPa, ultimate tensile strength = 588 MPa, and elongation = 14.8% for extrusions made from homogenized billets. T5 has not standard because it is impossible with conventional extrusion.
- Extrusion of 2024 at 7.4 meters/min compared to 3.5 meters/min for conventional extrusion.
- Achieved 2024-T8510 yield strength = 510 MPa, ultimate strength = 522 MPa, and elongation = 7.1% for extrusions made from wrought billets. Exceeds the ASTM and ASM standard, and typical industry values.
- Extrusion of Al-12.4TM high-performance aluminum powder directly into tubing, in a single step, which eliminates process steps typical of powder metallurgy extrusion.

Acknowledgments

The authors thank the U.S. Department of Energy Advanced Manufacturing Office (DOE/AMO) for their vision and support of this work to develop a new, low energy, manufacturing approach for high strength aluminum alloys. The Pacific Northwest National Laboratory is operated by the Battelle Memorial Institute for the United States Department of Energy under contract DE-AC06-76LO1830.

Acronyms and Abbreviations

ADF	Annular Darkfield
BC	Band Contrast
BF	Bright Field
CW	Cold Work
DF	Darkfield
DOE	Department of Energy
DDRX	Discontinuous Dynamic Recrystallization
EBSD	Electron Backscatter Diffraction
EDS	Energy Dispersive Spectroscopy
ER	Extrusion Ratio
EV	Electric Vehicle
FSBE	Friction Stir Back Extrusion
GDRX	Geometric Dynamic Recrystallization
HAGB	High Angle Grain Boundary
HRC	Rockwell Hardness Measured on the C Scale
ID	Inner Diameter
IPF	Inverse Pole Figure
KAM	Kernel Average Misorientation
LAGB	Low Angle Grain Boundary
LMP	Low Melting Point Phases
NREL	National Renewable Energy Laboratory
OD	Outer Diameter
PM	Powder Metallurgy
PNNL	Pacific Northwest National Laboratory
SE	Secondary Electron
SEM	Scanning Electron Microscopy
ShAPE	Shear Assisted Processing and Extrusion
SPD	Severe Plastic Deformation
STEM	Scanning Transmission Electron Microscopy
TC	Thermocouple
TEM	Transmission Electron Microscopy
TM	Transition Metal
UTS	Ultimate Tensile Strength
YS	Yield Strength

Contents

Executive Summary	iii
Acknowledgments	iv
Acronyms and Abbreviations	v
1.0 Introduction	1
2.0 Background	3
3.0 Experimental Approach	5
3.1 Equipment	5
3.2 Tooling	6
3.3 Quench System	8
3.4 Feedstock Materials	9
3.5 Heat Treatment	10
3.5.1 T6 temper for 7075 billets	10
3.5.2 T5 temper for 7075 billets	10
3.5.3 T3510 temper for 2024 billets	10
3.5.4 T8510 temper for 2024 billets	10
3.5.5 Al-12.4TM powder	10
3.6 Tensile Testing	10
3.7 Hardness Testing	11
3.8 Microstructural Characterization	11
4.0 Results	12
4.1 ShAPE Extrusion of 7075 Homogenized Billets	12
4.1.1 Mechanical Testing	12
4.1.2 Microstructural Characterization	15
4.2 ShAPE Extrusion of 7075 Unhomogenized Billets	19
4.2.1 Mechanical Testing	19
4.2.2 Microstructural Characterization	20
4.3 ShAPE Extrusion of 7075 with Quenching	26
4.4 ShAPE Extrusion of 2024	27
4.4.1 Mechanical Testing	27
4.4.2 Microstructural Characterization	30
4.5 ShAPE Extrusion of Al-12.4TM Powder	37
4.5.1 Mechanical Testing	37
4.5.2 Microstructural Characterization	38
5.0 Benefits Assessment	43
6.0 Publications	44
7.0 Intellectual Property	45
8.0 Awards and Recognition	46

9.0 Concluding Remarks 47
10.0 Recommendations 48
11.0 References 49

Figures

Figure 1. Schematic of ShAPE process for extruding aluminum alloy tubing.	1
Figure 2. 7075 tubing extruded by ShAPE.....	2
Figure 3. 2024 tubing extruded by ShAPE.....	4
Figure 4. ShAPE Machine manufactured by Bond Technologies, Inc. for PNNL.	5
Figure 5. a) Tooling mounted in ShAPE machine. b) Billet container mounted on crosshead. c) Extrusion die and holder mounted on rotating spindle. d) Die inserted into container prior to starting an extrusion trial.	6
Figure 6. Tooling utilized during ShAPE extrusion of aluminum alloys.	7
Figure 7. a) Quench tube inserted into the rotating spindle of the ShAPE machine. b) Cut-away showing water inlet, outlet, and location where the extrusion is cooled. c) Detail of shell and tube design with integrated quench ring near the die exit. d) Water spray in action.	8
Figure 8. (a) UTS and YS for 7075 tubing fabricated at different extrusion speeds with die temperature held constant near 420 °C (Trials 1–5 in Table 3) and heat-treated to the T6 condition. (b) Corresponding tube appearance.....	13
Figure 9. (a) Extrusion speed of 7075 for the ShAPE process (triangles) and conventional linear extrusion (circles). (b) 7075 tubing showing a typical surface at 12.2 m/min (ER = 33.9) and surface tearing at 13.9 m/min (ER = 40) from Trials 12 and 13 in Table 3.	14
Figure 10. Figure 4. (a) UTS and YS for 7075 tubing fabricated at different die temperatures with extrusion speed held constant at 7.4 m/min (Trials 5–10 in Table 1). (b) Corresponding tube appearance with surface tearing observed at 466 °C.....	15
Figure 11. SEM EDS was used to identify the larger precipitates that were solutionized after heat treatment. Compositional information from the 2.5 m/min low speed extrusion is presented in Figure 6 to illustrate the effects of heat treatment further. Considerable dissolution of LMP AlMgCuZn-rich second phases is evident when single element maps are compared before (ShAPE Processed) and after heat treatment (ShAPE + T6).....	16
Figure 12. EBSD inverse pole figure maps from longitudinal tube cross sections show considerable grain growth following T6 heat treatment.	16
Figure 13. EBSD disorientation angle distribution plots show significant changes in the relative frequency of low angle disorientation as a function of processing condition. A typical Mackenzie distribution is shown in gray.	17
Figure 14. STEM (ADF and BF) images illustrating microstructures of the T6 heat-treated alloys following extrusion at low (341 °C) vs. high (441 °C) temperature. a,b) STEM (BF) images showing the density of secondary particles in the matrix for the low and high temperature extrusions, respectively. (c,d) STEM (ADF) images comparing the approximate dimensions of the GP zones as well as the coverage of the eta phase (MgZn ₂) on the Al ₁₈ Mg ₂ Cr ₃ precipitates. (e) high angle annular dark field (filtered) atomic column image showing the relative orientation of the eta phase to the Al matrix in the 341°C heat treatment exhibiting the orientation relationship $(0001)_{\eta} // (111)_{Al}$ and $\langle 10\text{-}10 \rangle_{\eta} // \langle 112 \rangle_{Al}$	18

Figure 15. Optical image displaying five distinct regions from top to bottom: (a) extruded microstructure, (b) processed zone, (c) transition zone II, (d) transition zone I, and (e) unhomogenized 7075 Al alloy base; EBSD analysis and SE images of selection regions (a)-(e).	21
Figure 16. Evolution of the misorientation distribution histograms throughout the microstructural regions of interest. These correspond to the locations labeled in Figure 15 as (a)-(e).	22
Figure 17. (a) BF- and (b,c) DF-TEM images of the grain-refinement region (location (c) labeled in Figure 15).	23
Figure 18. DF-TEM and EDS map of Al matrix and main alloying elements of Zn, Mg and Cu in grain refining region and base 7075.	23
Figure 19. Comparison of the alloying elements in the matrix between the unhomogenized base and the grain-refined region.	24
Figure 20. Secondary phase variation during deformation. (a) and (e) BF-TEM images showing the initial spindle and the deformed irregular morphology of MgZnCu particles in the base region and the processed zone, respectively. (b) and (f) SAED patterns showing the single crystalline and polycrystalline structures of the MgZnCu phases in (a) and (e), respectively. (c) and (g) High-Resolution TEM image showing the crystalline and amorphous structures of the E phases, respectively. (d) and (h) HAADF-STEM images of the Al matrix.	24
Figure 21. TEM-EDS mapping of the particles in Figure 20(a) and (e).	24
Figure 22. (a) Extrusion ram force and (b) die temperature, and (c) surface appearance of ShAPE extruded tubes at different die temperature.	28
Figure 23. Stress-strain curves of as received 2024-T351 precursor and ShAPE extruded 2024-T6 tube.	29
Figure 24. Stress-strain curves of 2024 tube after different post extrusion tempering including T6, T3510 and T8510.	29
Figure 25. Comparison of tensile properties of different tempered 2024 ShAPE extruded tubes and relevant standard values: (a) ultimate tensile strength, (b) 0.2% yield strength, and (c) % elongation.	30
Figure 26. EBSD analyses of transverse and longitudinal microstructures of 2024: (a) As-received 2024-T351 bar with schematic orientation of transverse and longitudinal section, (b) transverse grain microstructures of as-received bar, (c) longitudinal grain microstructures as-received bar, (d) ShAPE extruded 2024 tube with schematic orientation of transverse and longitudinal section, (e) transverse grain microstructures of ShAPE extruded tube, (f) longitudinal grain, microstructures of ShAPE extruded tubes.	31
Figure 27. Grain microstructures of 2024 ShAPE extruded tubes from EBSD IPF after different post extrusion heat treatment: (a) transverse T3510 (3.5% CW), (b) transverse T3510 (4.5% CW), (c) transverse T8510 (3.5% CW), (d) transverse T8510 (4.5% CW), (e) longitudinal T3510 (3.5% CW), (f) longitudinal T3510 (4.5% CW), (g) longitudinal T8510 (3.5% CW), (h) longitudinal T8510 (4.5% CW).	32
Figure 28. SEM images highlighting bright second phase precipitates in the transverse and longitudinal sections of 2024 ShAPE tubes after different post	

extrusion heat treatment: (a) T3510 (3.5% CW), (b) T3510 (4.5% CW), (c) T8510 (3.5% CW) and (d) T8510 (4.5% CW)..... 33

Figure 29. SEM EDS mapping illustrating the S phase in longitudinal sections of 2024 ShAPE tubes after different post extrusion heat treatment: (a) T3510 (3.5% CW), (b) T3510 (4.5% CW), (c) T8510 (3.5% CW) and (d) T8510 (4.5% CW). 34

Figure 30. High resolution SEM BSE images with Cu, Mg and Mn mapping for 2024 tubes with (a) T3510-3.5% cold working and (b) T8510-4.5% cold working. 35

Figure 31. ShAPE process parameters used for manufacturing Al-12.4TM tubes in one-step approach and the corresponding extrusion forces, torque and temperatures observed during manufacturing..... 37

Figure 32. Surface features on the Al-12.4TM ShAPE tubes manufactured at an extrusion ratio of 20.6 and feed rates varying from 8 – 60 mm/min. 38

Figure 33. Density (A) and Vickers hardness (B) of Al-12.4TM ShAPE tubes products made with different feed rates. 38

Figure 34. Top, An optical overview image of half of the longitudinal cross-section of the remnant precursor and the last part of the extruded tube, 42 rpm, 8 mm/min. Bottom, high magnification SEM images at locations 1-4 on the overview image. 39

Figure 35. SEM of the ShAPE tubes made with different feed rates. (a) 8 mm/min, outer diameter; (b) 8 mm/min, inner diameter; (c) 45 mm/min, outer diameter; (d) 45 mm/min, inner diameter. Labelled with average Vicker’s hardness. Inserts are higher magnification images with the length scale representing 5 μm. 41

Tables

Table 1. Composition of 7075 ingots as wt%.....	9
Table 2. Composition of wrought 2024 as wt%.....	9
Table 3. Process parameters for ShAPE extrusion of 7075 homogenized billets.....	12
Table 4. Summary of mechanical properties for ShAPE extrusions from homogenized billets compared to the ASTM and ASM values for conventional extrusion.	15
Table 5. TEM findings 341 °C and 441 °C process temperature comparison in the T6 condition.	18
Table 6. Process parameters for ShAPE extrusion of 7075 unhomogenized billets.....	19
Table 7. Summary of mechanical properties for ShAPE extrusions from unhomogenized billets compared to the ASTM and ASM values for conventional extrusion.	19
Table 8. Parameters for ShAPE extrusion of 7075 homogenized and unhomogenized billets.	26
Table 9. Tensile properties of ShAPE extruded 7075, from homogenized and unhomogenized billets that underwent artificial aging without solution heat treating first.....	26
Table 10. Process parameters for ShAPE extrusion of 2024-T351 billets.....	27
Table 11. Grain size of ShAPE extruded and as-received 2024 tubes with different heat treatment.	33

1.0 Introduction

The overarching goal of this project was to demonstrate that Shear Assisted Processing and Extrusion (ShAPE) can manufacture high-performance aluminum alloy tubing with lower embedded energy and improved mechanical properties compared to conventional extrusion. Development of the ShAPE manufacturing process, mechanical testing, and microstructural characterization were performed by PNNL and are reported herein. A techno-economic and energy analysis comparing ShAPE with conventional extrusion was performed by NREL and is documented in a separate report [1].

Unlike conventional extrusion where the billet is rammed against a stationary die using a strictly linear motion, the ShAPE process superimposes a rotational shear force by spinning the die while the billet is plunged (Figure 1) [2]. Contact between the billet and rotating die generates heat due to friction and plastic deformation within the deforming material. As temperature increases, material flows inward toward the extrusion orifice, assisted by spiral grooves on the die face, and then between the mandrel and die to form an extruded tube. The extent of heat generation and deformation are controlled by regulating rotational speed and ram speed, with motor torque and ram force following to achieve the commanded speeds [3]. Compared to conventional linear extrusion, the ShAPE process imparts significantly more strain into the feedstock material, akin to severe plastic deformation (SPD) techniques, which enables the formation of novel microstructures. These microstructures manifest an array of benefits that underpin a variety of improvements such as and improved material properties and reduced process energy compared to conventional extrusion.

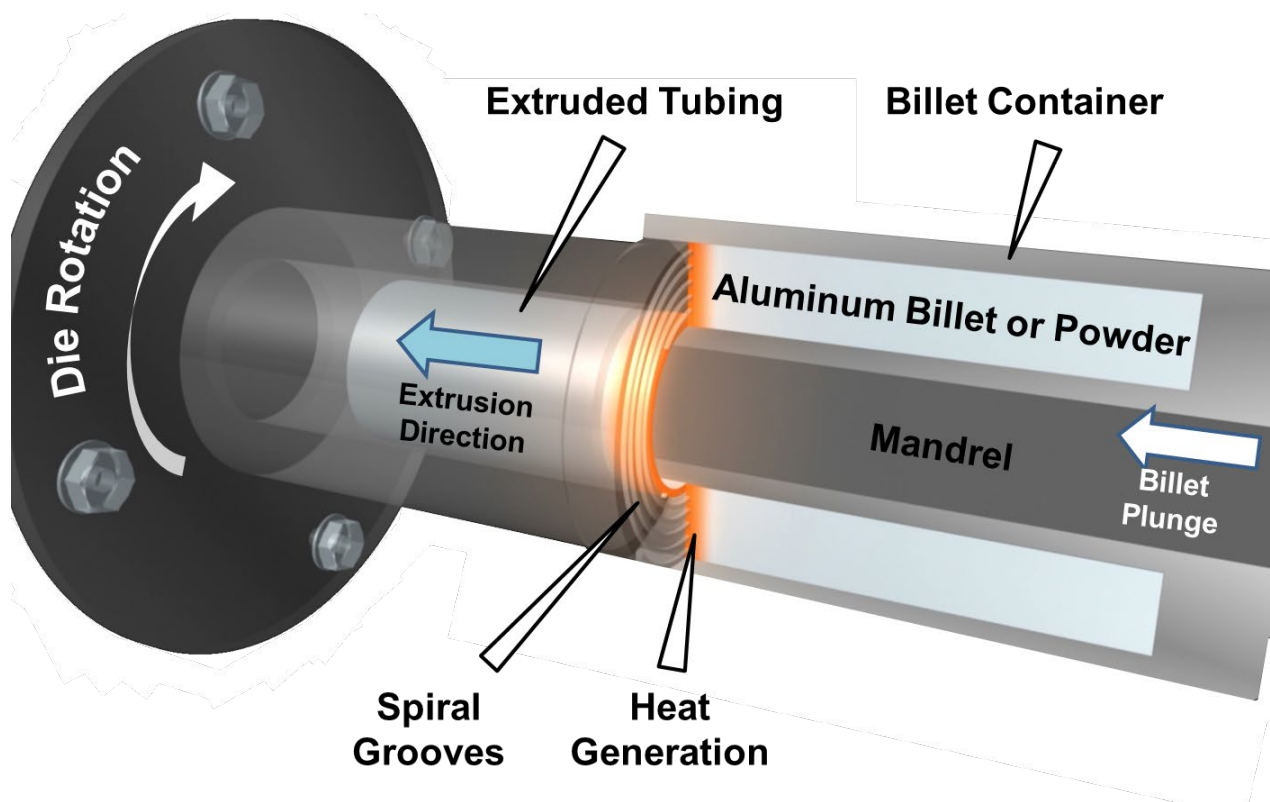


Figure 1. Schematic of ShAPE process for extruding aluminum alloy tubing.

This project focused on aluminum aerospace alloys 7075 and 2024 which rank among the most difficult to extrude aluminum alloys [4]. Improved manufacturability and cost reduction of these, and other, high-performance alloys could enable widespread use in more cost sensitive industries such as the automotive sector. The extrusion process, heat treatment steps, and mechanical properties of these two alloys have remained largely unchanged since the 7075 was first standardized for aerospace use in 1945 [5] and 2024 was first introduced by Alcoa in 1931 [6]. Gas-atomized Al-12.4TM aluminum alloy powder was also investigated to demonstrate process efficiencies for ShAPE compared to conventional powder metallurgy extrusion. Whether by increased throughput, reduced heat treatments, or elimination of process steps; the ShAPE technology invented and developed by PNNL [7] has the potential to dramatically reduce energy consumption in the aluminum extrusion industry while simultaneously achieving improved mechanical properties compared to conventional extrusion.



Figure 2. 7075 tubing extruded by ShAPE.

The global market size for aluminum extrusions was 28.08 million metric tons in 2020 and is projected to accelerate at approximately 4% annually, reaching a volume of 35.47 million metric tons by 2026 [8]. A primary contributor to this growth is expected to be the electric vehicle (EV) market where high-performance aluminum alloy extrusions are needed. This represents a large opportunity for energy savings where ShAPE can be used to extrude structural components for EVs such as battery trays. PNNL is aggressively protecting intellectual property in this area as part of a commercialization strategy. Over the course of this project, two non-provisional patents have been filed [9,10] with two provisional patents [11,12] in the process of converting to non-provisional filings. Selected results from this project have been shared with companies in the aerospace, automotive, and powder supply industries and opportunities are being explored to mature the ShAPE technology for a range of applications, materials, and profile geometries. Discoveries made on this project have enhanced other currently funded DOE projects at PNNL and have laid the foundation for future work being proposed with industry partners. Round tubing was manufactured for this project (Figure 2) and PNNL is now developing the capability of ShAPE for non-circular profiles such as square, rectangular, and trapezoidal shapes, and potentially multi-cell profiles.

2.0 Background

The most common aluminum alloys utilized in the aerospace industry are 7075 and 2024 due to their high strength-to-weight ratio compared to advanced high strength steels and other aluminum alloys [13]. Lightweight structures are also of interest to the automotive industry since reducing vehicle weight by 45 kg can result in a 1-2% improvement in fuel efficiency [14], which in turn reduces CO₂ emissions by approximately 70 kg/yr for a typical passenger vehicle [15]. Despite this opportunity, 7075 and 2024 have seen limited use outside of the aerospace industry due in part to high cost. However, if 7075 and 2024 extrusions could be made more cost competitive by eliminating energy intensive process steps typical of conventional extrusion, then numerous opportunities exist for more widespread adoption [16].

A key reason for the high cost of 7075 and 2024 extrusions (25-75% higher than 6061) [17] is that these alloys are difficult to extrude. 7075 is characterized as the number one least extrudable of 25 commonly available aluminum alloys and 2024 is ranked eighth based on criteria such as material properties, profile geometry, surface finish, ram pressure, and extrusion speed [4]. Of these factors, a primary contributor to the high cost is slow extrusion speed with 7075 and 2024 limited to 0.8-2 m/min and 1.5-3.5 m/min respectively [18]. This is in comparison to 6061 which can be extruded at 20–100 m/min [19]. The technical barriers limiting the extrusion speed of 7075 and 2024 primarily involve surface tearing due to incipient melting of low melting point (LMP) phases [20], abnormal grain growth [21], and material flow phenomena [22].

In addition to slow speed, aluminum alloys require numerous thermal treatments throughout the extrusion process including homogenization and pre-heating prior to extrusion, and solution heat treating and artificial aging after extrusion [22]. Each of these steps contribute to the total energy consumed during manufacturing of extruded components. This project investigates the use of ShAPE to improve extrusion speed and reduce, or even eliminate, the typical thermal treatments for high strength aluminum alloys. Most of the research during this project was performed on 7075 and only applied to 2024 near the end of the project.

Specialty aluminum powders made by rapid solidification are also of interest as extruded components due to their potential for high strength [23] and improved thermal stability [3]. However, the manufacturing pathway to convert loose powder into a consolidated extrusion by powder metallurgy (PM) contains many process steps and is not cost-effective for mass market components. For example, PM of high strength aluminum alloys typically require multiple process steps prior to extrusion [24]. In general, the most widely utilized methods to prepare material for PM extrusion are compacting powder into a densified billet or canning powder in a sealed container [25,26]. For canning, typical steps include loading powder into a can, degassing, sealing, and heating. For powder compaction, typical steps include degassing, hot or cold isostatic pressing, and heating the densified billet. Eliminating any of these canning or compaction steps prior to extrusion would consume less process energy thereby making PM more cost effective and less energy intensive. This project investigates the use of ShAPE to consolidate Al-12.4TM gas-atomized aluminum powder directly into an extruded tube, in a single step, thereby reducing energy through elimination of numerous process steps typical of PM extrusion.

Improved material properties for aluminum alloys manufactured by SPD techniques, of which ShAPE can be considered one, have been widely documented in the literature cited within this report. The reader is referred to the noted review articles for a myriad of examples highlighting improvements to mechanical and functional properties via SPD of aluminum alloys [27-29]. In general, these property advancements result from extensive grain refinement coupled with the breakdown and uniform dispersion of second phases. Although interesting from an academic perspective, SPD techniques hold little value for industry since they are not readily scalable. In contrast, ShAPE has garnered extensive industry interest precisely because the process is scalable (Figure 3), while retaining the material property benefits of SPD that result from extreme microstructural refinement of the aluminum matrix and second phases.

ShAPE is sometimes confused with the Friction Stir Back Extrusion (FSBE) method for fabricating hollow profiles which was first proposed in 2012 [30]. A key difference is that, for FSBE, the extruding material flows onto a rotating mandrel rather than off a stationary mandrel as occurs during ShAPE. As a result, the extrusion length for FSBE is constrained by the length of the rotating mandrel and the longest extrusion reported to date is 12 cm [31]. A complication of FSBE is that the tube must somehow be removed from the outer diameter of the rotating mandrel after extrusion is complete which is not practical for manufacturing. Additionally, the tooling configuration of FSBE does not permit large extrusion ratios (ER) due to unfavorable implications on machine torque required to drive the process. As a result, the largest extrusion ratio found in the literature for FSBE is 2.8 [32] which limits the extent of shear imparted to the material. Low ER also results in slow extrusion speed with the highest reported value in the literature being 0.24 m/min [33], which is 5-10 times slower than conventional extrusion of 7075 and 2024. Also, FSBE is not capable of a porthole bridge die approach like ShAPE is, which is required for non-circular and multi-cell profiles needed by industry. Due to these factors, FSBE is not scalable to an industry level.

The remainder of this report details the research approach and scientific advances discovered for ShAPE extrusion of aluminum 7075 billets, 2024 billets, and Al-12.4TM powder. Consideration will be given to tooling design and fabrication, ShAPE extrusion process development, mechanical tensile testing, and microstructural characterization. Where possible, comparisons will be made with state-of-the-art for conventional extrusion. Quantification of energy savings achieved using the ShAPE process are documented in a separate report [1].



Figure 3. 2024 tubing extruded by ShAPE.

3.0 Experimental Approach

3.1 Equipment

Extrusions were fabricated using a purpose-built ShAPE machine manufactured by Bond Technologies, Inc. located in Elkhart, IN. The ShAPE machine, shown in Figure 4, is the first-of-its-kind in the world specifically built for manufacturing extrusions using the ShAPE process. The machine was already in service at PNNL when the project was awarded and was not procured as part of this project.

The ShAPE machine consists of a rotating spindle and traversing crosshead, or ram. The spindle is capable of rotating at 200 rpm with 3000 Nm of torque. Actuated by two hydraulic rams capable of 900 kN in total, the crosshead is capable of a 360 mm/min ram speed. For experiments performed on this project, spindle rpm and ram speed were the control variables with spindle torque and ram force being the response variables. Like a lathe, the speeds and feeds are fully programmable, yet can also be actively controlled during the experiments. It is these process parameters that affect the amount of shear deformation imparted to the material, the temperature during deformation, and ultimately the microstructural characteristics and bulk mechanical properties. Additionally, the process parameters affect production rate and quality of the extruded tubing.



Figure 4. ShAPE Machine manufactured by Bond Technologies, Inc. for PNNL.

3.2 Tooling

The tooling required for extrusion was designed, fabricated, and mounted inside the working area of the ShAPE machine as shown in Figure 5. Figure 5a shows the extrusion die and die holder mounted onto the rotating spindle and the billet container mounted on the traversing crosshead. The billet container shown in Figure 5b was designed to withstand the full torque and force of the ShAPE machine at a temperature of 500 °C to ensure functionality in the most extreme condition that could be encountered. The billet container was fully engineered using structural and thermal finite element analysis to design the container which consists of brazed and welded stainless steel and brass components to optimize strength and thermal transport. The billet container is internally water cooled so that temperature can be quickly lowered after extrusion to enable fast turn-around between experiments. Argon was used as the inert cover gas for all experiments to minimize elevated temperature reactions. The mandrel, billet, and liner are housed within the billet container and are discussed in Figure 6. Figure 5c shows the extrusion die mounted inside of a die holder fabricated from fully hardened H13 tool steel, with a wireless thermocouple transmitter for collecting in-process temperature data at the surface of the scrolled face on the extrusion die. Figure 5d shows the extrusion die inserted into the billet container prior to starting the extrusion process. The container was designed for compatibility with solid billets and powder feedstock.

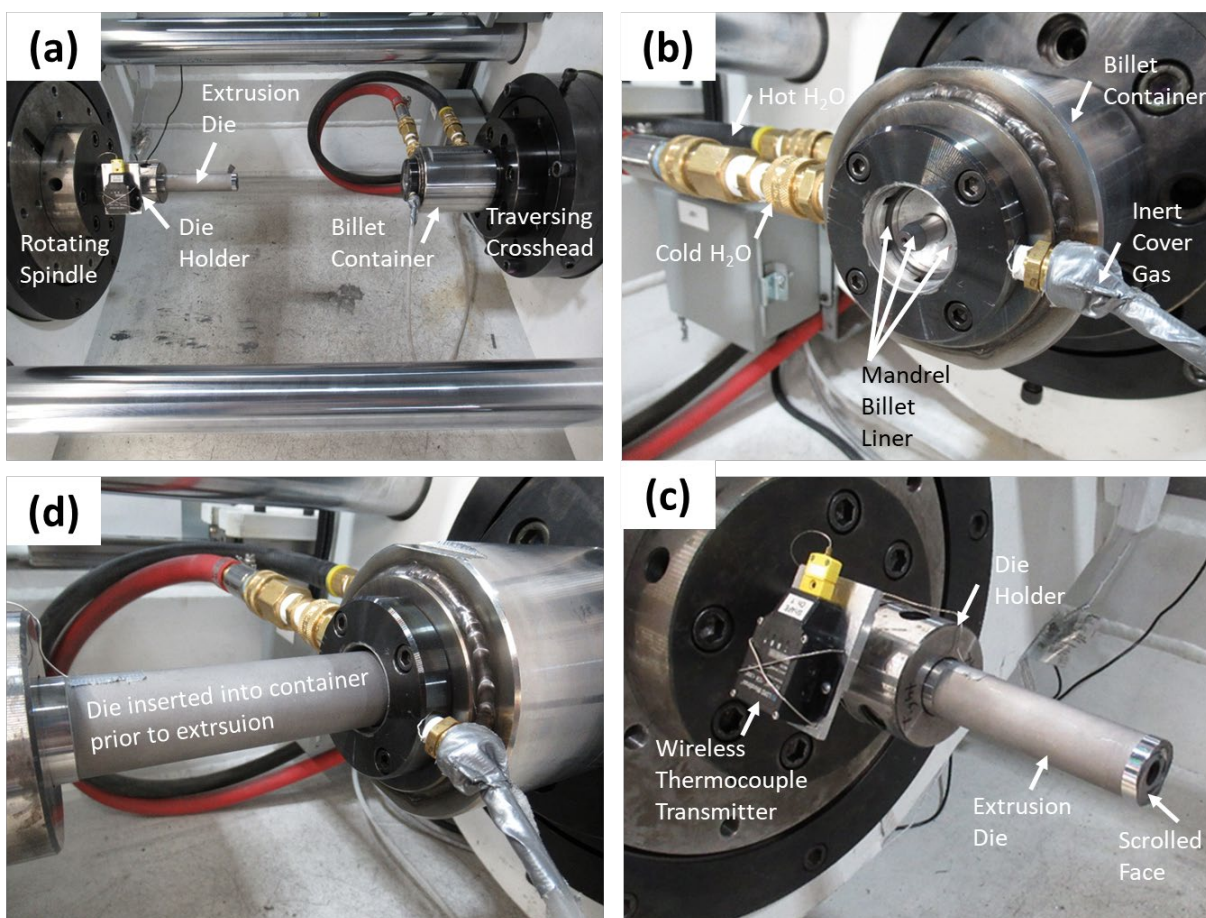


Figure 5. a) Tooling mounted in ShAPE machine. b) Billet container mounted on crosshead. c) Extrusion die and holder mounted on rotating spindle. d) Die inserted into container prior to starting an extrusion trial.

Figure 6a shows the extrusion die along with the mandrel, solid billet, and liner that were indicated as being internal to the billet container in Figure 5c. These pieces are directly involved during the ShAPE extrusion process and warrant a more detailed discussion here. The extrusion die, mandrel, mandrel base, and liner were fabricated from H13 tool steel heat treated to Rockwell hardness > 50 measured on the C scale (HRC) in order function in the elastic range at 500 °C under the full torque and force capacity of the ShAPE machine.

Figure 6b shows a cut-away of the die head indicating the key features. The spiral scrolled face is design to capture the deforming material and direct flow inward toward the extrusion orifice. A type-K thermocouple (TC) is spot welded at the base of a scroll located midway between the inner diameter (ID) and outer diameter (OD) of the die face for the purpose of measuring temperature as close to the deforming material as possible. This thermocouple is used as a process variable against which the rpm is controlled to achieve steady state temperature during extrusion. A counterbore feature was incorporated to provide a reservoir for material streams to consolidate after exiting the scrolled features. A slight relief was included on the OD of the die to minimize friction between the die and liner. The bearing surface has a diameter of 12 mm which sets the OD of the extruded tubing. Bearing length was minimized to keep extrusion force as low as possible while still providing sufficient back pressure to ensure full consolidation of the tubing.

The billet liner has an ID of 31.8 mm which sets the OD of the billet. The OD of the liner is keyed with slots that prevent rotation of the liner relative to the billet container, which has the inverse slot pattern. The mandrel has a diameter of 10 mm which sets the ID of the extruded tubing. The mandrel base accommodates the mandrel and rotation between the mandrel and base are prevented using a dowel pin that locks the pieces together. Keys in the mandrel base also prevent rotation relative to the billet container. Aluminum billets were machined to a length of 102 mm, OD of 38.1 mm, and ID of 10 mm with appropriate tolerancing to allow slip fits with the liner OD and mandrel ID. The central hole in the billet approximates a pierced billet that would typically be used in a commercial extrusion process. In the case of powder, the space between the OD of the mandrel and ID of the liner was loaded with loose powder prior to extrusion. In this configuration, the extrusion ratio (ER) is 20.6, calculated as the area of the billet face divided by the cross-sectional area of the extruded tubing. For one subset of experiments with solid billets, mandrel diameters of 10.85 mm and 11 mm were used to explore higher extrusion ratios of 33.9 and 40.0 respectively.

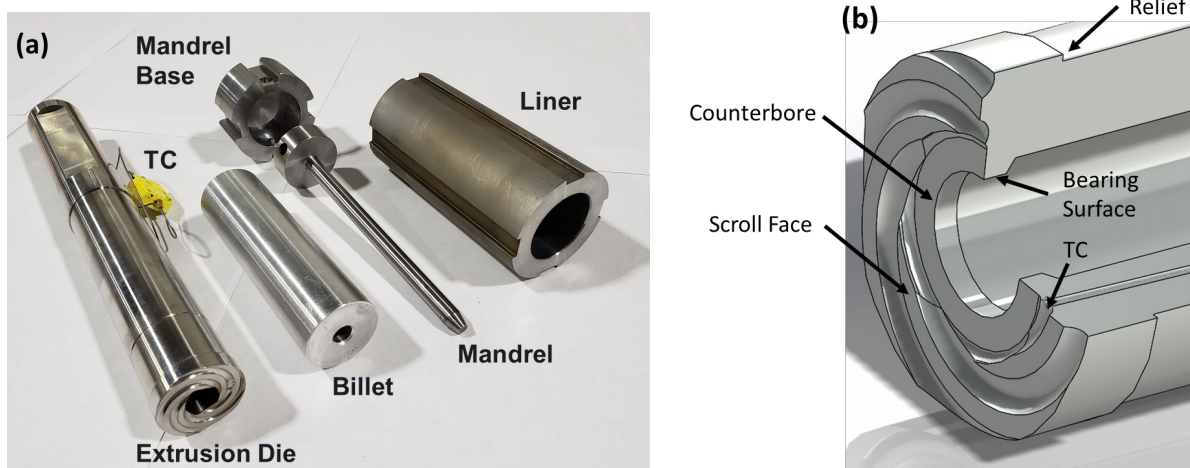


Figure 6. Tooling utilized during ShAPE extrusion of aluminum alloys.

3.3 Quench System

Aluminum alloy 7075 is extremely quench sensitive; meaning that strengthening precipitates form and rapidly coarsen while the extrusion cools, which degrades mechanical properties. 7075 is so quench sensitive that even immediate water quenching does not achieve a fast enough cooling rate during conventional extrusion because the extrusion speed is too slow (0.8-2 m/min). Because of this phenomenon, 7075 must be solution heat treated (1 hour at 480 °C), water quenched, and then artificially aged (24 hours at 120 °C) after extrusion to achieve the popular typical T6 temper. In aluminum alloys with low quench sensitivity, such as 6061, water quenching immediately after the extrusion exits the die, combined with an extremely high extrusion speed (>20 m/min) enables what is known as “press quenching” where the solution heat treatment and quench steps occur in situ during the extrusion process. It was hypothesized that press quenching could be achieved for 7075 if 1) ShAPE achieved higher speeds than conventional extrusion and 2) a water quench system is integrated into the rotating spindle of the ShAPE machine to cool the extrusion immediately after it exits the die. To that end, a unique, patent pending, quench system was designed, fabricated, and installed for this project and shown in Figure 7. Development of the quench system did not occur until late in the project and thus was only utilized on a small subset of experiments.

In Figure 7a, the quench tube is shown inserted through the rotating spindle during a ShAPE extrusion trial. A cut-away of the quench tube is shown in Figure 7b with the water inlet and outlet specified. The dashed box indicates the section of the quench tube where the extrusion is cooled and is magnified in Figure 7c. The design consists of an inner tube and outer shell that are capped with a circular quench ring containing 16 individual spray nozzles. Cold water flows between the OD of the inner tube and ID of the outer shell toward the exit of the extrusion die where it sprays through the nozzles. Hot water is returned to the reservoir by draining through the inner tube. Figure 7d shows the water jets in action. Based on the extrusion speeds obtained for 7075 on this project, the extrusion reaches the quench ring in approximately 2 seconds; long before deleterious effects of slow cooling have degraded properties.

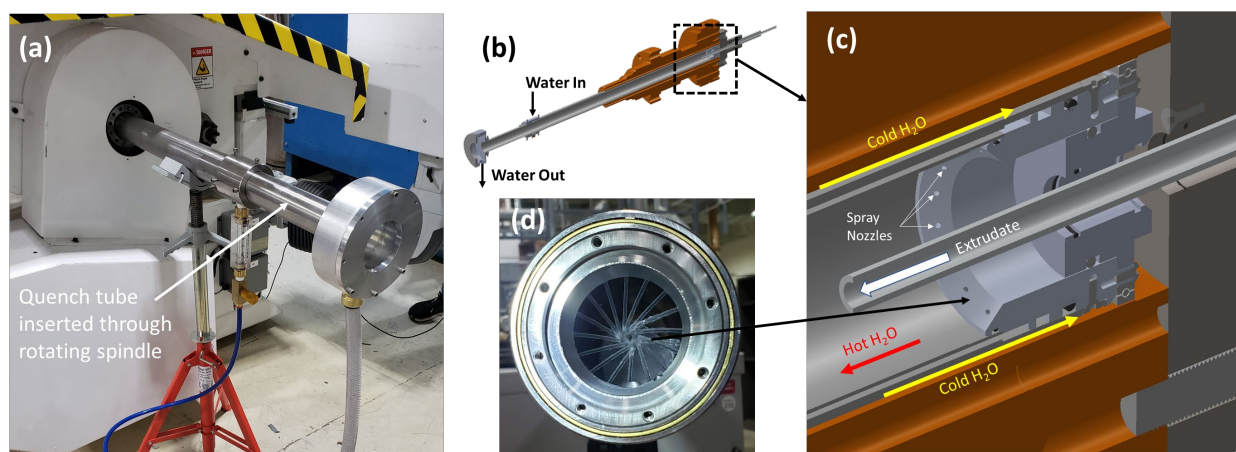


Figure 7. a) Quench tube inserted into the rotating spindle of the ShAPE machine. b) Cut-away showing water inlet, outlet, and location where the extrusion is cooled. c) Detail of shell and tube design with integrated quench ring near the die exit. d) Water spray in action.

3.4 Feedstock Materials

Aluminum alloy 7075 ingots were provided to PNNL in the homogenized and unhomogenized conditions. PNNL then machined the ingots into the billet geometry described in Figure 6a. The composition of the ingots is shown in Table 1. Unhomogenized ingots were in the as-cast condition plus a gentle stress relief heat treatment for approximately 6 hours at 370 °C. Homogenized ingots underwent an additional heat treatment for approximately 20 hours at 430 °C. Homogenized and unhomogenized billets were from the same parent casting. Homogenized billets were investigated because they represent the feedstock material utilized by the extrusion industry. This enabled a side-by-side comparison of manufacturing speeds and mechanical properties for ShAPE and conventional extrusion. Unhomogenized billets, which are not extrudable by conventional extrusion, were also investigated. It was hypothesized that the extreme shear imparted during ShAPE could perform homogenization in situ during the extrusion process, thereby eliminating the need for the energy intensive homogenization thermal treatment.

Table 1. Composition of 7075 ingots as wt%.

Al	Si	Fe	Cu	Mn	Mg	Cr	Zn	Ti	V	Zr	Ca	B	Na	Pb	Be	Li	Ni
Bal.	0.07	0.17	1.54	0.04	2.43	0.20	5.65	0.03	0.01								<0.005

Wrought aluminum alloy 2024 was provided to PNNL in the T351 condition. PNNL then machined the wrought product into the billet geometry described in Figure 6a. The composition of the ingots is shown in Table 2. Wrought 2024 was utilized because this alloy was not investigated until late in the project and a source for homogenized and unhomogenized ingots was not able to be identified in time.

Table 2. Composition of wrought 2024 as wt%.

Al	Si	Fe	Cu	Mn	Mg	Cr	Zn	Ti	V	Zr	Ca	B	Na	Pb	Be	Li	Ni
Bal.	0.50	0.50	3.80-4.90	0.30-0.90	1.20-1.80	0.10	0.25	0.10									<0.05 each and <0.15 total

Al-12.4 wt% transition metal (TM) powder, referred to as Al-12.4TM, was provided by SCM Metal Products, Inc. a division of Kymera international. This powder was produced by induction melting followed by inert gas atomization and subsequently screened to < 400 µm. The powder was stored in an ambient air environment prior to extrusion and was utilized in the as-received condition. The powder contains 12.4 wt% of transition metals Ti, Cr, Mn, Mo, Fe, Si and other additives with the balance being Al. Additional detail on the powder can be found in the is reference [34].

3.5 Heat Treatment

3.5.1 T6 temper for 7075 billets

Tubes were stored in a freezer at -52 °C immediately after extrusion to minimize the effects of natural aging. Extrusions were tempered to the T6 condition by solution heat treating at 480 °C for 1 hr followed by water quenching and then artificial aging at 120 °C for 24 hr. Heat treatment was performed using a Neytech Vulcan 3-550 multi-state programmable furnace with an ambient environment.

3.5.2 T5 temper for 7075 billets

Tubes were stored in a freezer at -52 °C immediately after extrusion to minimize the effects of natural aging. Extrusions were tempered to the T5 condition by artificial aging at 120 °C for 24 hr. Heat treatment was performed using a Neytech Vulcan 3-550 multi-state programmable furnace with an ambient environment.

3.5.3 T3510 temper for 2024 billets

Tubes were stored in a freezer at -52 °C immediately after extrusion to minimize the effects of natural aging. Extrusions were tempered to the T3510 condition by solution heat treating at 495 °C for 1 hr, immediately water quenched, then strain hardened to 4.5% by stretching, followed by natural aging at room temperature for 30 days. Heat treatment was performed using a Neytech Vulcan 3-550 multi-state programmable furnace with an ambient environment.

3.5.4 T8510 temper for 2024 billets

Tubes were stored in a freezer at -52 °C immediately after extrusion to minimize the effects of natural aging. Extrusions were tempered to the T3510 condition by solution heat treating at 495 °C for 1 hr, immediately water quenched, then strain hardened to 4.5% by stretching, followed by artificial aging 190 °C for 10 hours. Heat treatment was performed using a Neytech Vulcan 3-550 multi-state programmable furnace with an ambient environment.

3.5.5 Al-12.4TM powder

Al-12.4TM is not a precipitation hardening alloy and therefore does not respond to heat treatment. Heat treatment was not performed on Al-12.4TM extrusions.

3.6 Tensile Testing

Tensile testing was performed on an MTS 22 kN servo hydraulic test frame per ASTM B557-15 [35], which specifies tensile testing of aluminum alloys including tubular cross sections. A crosshead displacement rate of 5.1 mm/min was used to assure quasi-static conditions. A Correlated Solutions stereoscopic digital image correlation system and VIC-3D analysis software were used to quantify strain. A black spray-painted speckle pattern was applied to the surface of the gage length to create the desired size and density of tracking subsets for resolving strain in three dimensions. Tensile specimens were 12.7 cm long with a 5 cm gage length.

3.7 Hardness Testing

Vicker's hardness was measured on the longitudinal cross-section of the Al-12.4TM tube from the outside diameter to the inside diameter of the tube with 200 μm intervals using 200 grams force and 12 seconds dwell time per ASTM E384.

3.8 Microstructural Characterization

Metallographic specimens for microstructural characterization were sectioned perpendicular (transverse) and parallel (longitudinal) to the extrusion direction, mounted in epoxy, and polished to a final surface finish of 0.05 μm using colloidal silica.

For 2024, scanning electron microscopy (SEM) was performed with a JEOL 7001F equipped with dual Bruker X-Flash 6-60 energy dispersive spectrometers (EDS), and a Bruker e-Flash electron backscatter diffraction (EBSD) detector. Bruker Esprit 2.1 software was used for all analysis of EDS and EBSD. EDS mapping conditions of 15 kV, probe current 13, aperture 4 and 10mm working distance were used for EDS map collection on all samples. EBSD maps were collected at 30kV, probe current 15 (adjusted to 35nA with the integrated probe current detector), aperture 2, 21mm working distance and a specimen tilt of 70°. Indexing of aluminum was performed using a cubic crystal system (IT# 225) with $a=b=c=4.049\text{Å}$ and $\alpha=\beta=\gamma=90^\circ$. Grain size reported is the maximum feret diameter (largest intercept between boundaries of a grain at any angular relation) after a post-processing operation requiring a minimum 25 pixels in a grain (0.76 μm per pixel) and a maximum misorientation of 15° between pixels to define the grain edge. Post-processing also allowed surrounded pixels to be absorbed into a grain, up to a maximum of 10 contiguous pixels.

For 7075 and Al-12.4TM, SEM was performed using a JEOL IT800 FESEM equipped with an Oxford Instruments Symmetry EBSD detector. Oxford Instruments AZtec Nanoanalysis v.4.3 was used for data acquisition in conjunction with AZtec Crystal v.2 for EBSD post processing and analysis. Microscopy was performed using an accelerating voltage of 20 keV, analytical probe current setting of 75, a working distance of ~26 mm and a specimen tilt of 70. The grain boundaries were defined as 10° disorientations. Grain size reported is the equivalent circular diameter for ShAPE processed specimens because an equiaxed grain size was observed. Alternately, for the heat-treated samples, grain size is reported as a feret diameter (largest intercept between boundaries of a grain at any angular relation) because significant microstructural elongation was observed. The reported feret diameter of these specimens should be understood as an under-estimation due to the elongated nature of this microstructure. EDS mapping was performed using a JEOL IT500 FESEM equipped with dual 100 mm² Oxford Instruments EDS detectors and analyzed using Oxford Instruments AZtec Nanoanalysis v.4.3. EDS data acquisition was performed at a 10 mm working distance, using a probe current setting of 85, a 10 keV accelerating voltage and 40 μm aperture.

Scanning transmission electron microscopy (STEM) was performed on an aberration C_s -corrected JEOL ARM200CF microscope operated at 200 keV, equipped with both a JEOL Centurio EDS, and a Gatan Orius CCD camera. Digital imaging data collection was achieved using Gatan Microscopy Suite (GMS version 3). Annular darkfield (ADF) imaging, brightfield (BF) imaging, and EDS were used to analyze samples prepared via focused ion beam milling conducted on either an FEI Quanta 3D or a Helios. STEM ADF images were collected with a convergence angle of 27.5 mR and a collection angle of 72–294 mR, and STEM BF images were collected with a convergence angle of 6.9 mR and a collection angle of 0–9 mR.

4.0 Results

4.1 ShAPE Extrusion of 7075 Homogenized Billets

4.1.1 Mechanical Testing

Table 3 shows the process parameters for 13 ShAPE extrusion trials designed to span a range of extrusion speeds and temperatures. Control variables were the ram speed and rotation speed while the response variables were extrusion speed and die temperature. The ER is multiplied by ram speed to calculate the extrusion speed. For a die temperature near 420 °C, extrusion speeds ranging from 2.5 to 7.4 m/min (Trials 1–5). For an extrusion speed of 7.4 m/min, die temperatures varied from 341 to 484 °C (Trials 5–11). To investigate the limit of extrusion speed, the mandrel diameter was increased to 10.85 and 11.00 mm to obtain an ER of 33.9 and 40.0 corresponding to extrusion speeds of 12.2 and 13.9 m/min respectively (Trials 12 and 13). The purpose of this experimental matrix was to investigate the effect of ShAPE processing on mechanical properties and microstructures over a range of extrusion speeds and temperatures. The die temperature and ram force are the steady values observed during the extrusion trials.

Table 3. Process parameters for ShAPE extrusion of 7075 homogenized billets.

	Extrusion Trial (#)	Ram Speed (m/min)	Extrusion Ratio	Extrusion Speed (m/min)	Rotation Speed (rpm)	Die Temperature (°C)	Ram Force (kN)	Ram Pressure (MPa)
Extrusion Speed	1*	0.12	20.6	2.5*	60	426	297	417
	2	0.18	20.6	3.7	70	422	338	474
	3	0.24	20.6	5.0	80	421	362	508
	4	0.30	20.6	6.2	90	424	398	558
	5*	0.36	20.6	7.4*	100	419	408	572
Temperature	6*	0.36	20.6	7.4	40	341*	572	802
	7	0.36	20.6	7.4	50	362	504	707
	8	0.36	20.6	7.4	60	388	496	696
	9	0.36	20.6	7.4	80	411	481	675
	10*	0.36	20.6	7.4	120	441*	366	513
	11	0.36	20.6	7.4	150	466	314	441
Extrusion Ratio	12	0.36	33.9	12.2	50	398	695	994
	13	0.36	40.0	13.9	80	419	526	755

*Extremes in extrusion speed (Trials 1 and 5) and temperature (Trials 6 and 10) were selected for microstructural characterization.

Tensile data for extrusions fabricated with a die temperature near 420 °C and extrusion speed ranging from 2.5 to 7.4 m/min is shown in Figure 8 (Trials 1–5 in Table 3). Ultimate tensile strength (UTS), yield strength (YS), and elongation are shown for the T6 condition (Figure 8a). Extrusion speed was not observed to have a significant impact on strength. UTS ranged from a low of 523.8 ± 5.0 MPa (Trial 4) to a high of 537.0 ± 3.8 MPa (Trial 5). YS ranged from a low of 438.9 ± 3.5 MPa (Trial 1) to a high of 465.7 ± 5.2 MPa (Trial 3). These values are slightly below the ASTM minimum standard of 540 MPa and 485 MPa for UTS and YS, respectively [36]. The marginally depressed strengths are likely due to the extrusion temperature being too low and the typical T6 solution heat treatment schedule not being optimized for ShAPE processed material. Heat treatment optimization is the subject of ongoing research. Elongation at break

ranged from a low of $12.2 \pm 1.1\%$ at (Trial 1) to a high of $14.5 \pm 0.9\%$ (Trial 4), which substantially exceed the 7% ASTM minimum standard [36] and 11% ASM typical values [37]. Helical surface markings were observed on the surface of ShAPE processed tubing (Figure 8b) in contrast linear markings in the extrusion direction common to conventional extrusion. With ShAPE, the pitch depends on the combination of extrusion speed and rpm. For example, Trial 1 was performed at 60 rpm and 2.5 m/min (42 mm/rev), while Trial 5 was performed at 100 rpm and 7.4 m/min (74 mm/rev). The periodicity of the helical surface markings for Trial 5 is approximately twice that of Trial 1 as visually evident in Figure 8b.

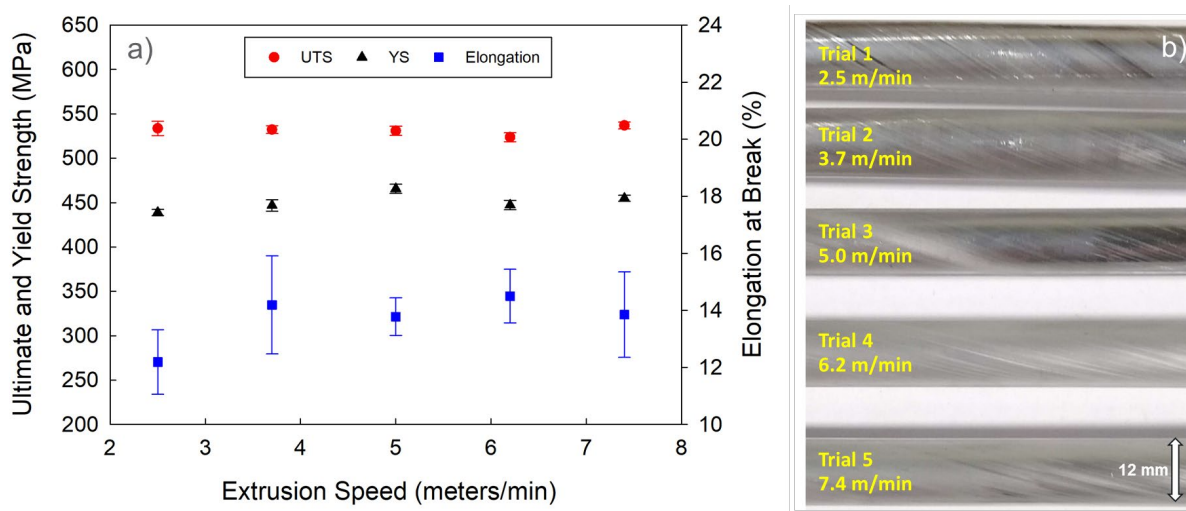


Figure 8. (a) UTS and YS for 7075 tubing fabricated at different extrusion speeds with die temperature held constant near 420 °C (Trials 1–5 in Table 3) and heat-treated to the T6 condition. (b) Corresponding tube appearance.

It is important to recall that the maximum extrusion speed for 7075 using conventional linear extrusion, without surface tearing or racking, is approximately 2 m/min [18,19,38-40]. Here, the ShAPE process is capable of substantially faster extrusion speeds while nearly maintaining ASTM mechanical properties.

ERs of 33.9 and 40.0 were also investigated to achieve extrusion speeds of 12.2 and 13.9 m/min respectively (Trials 12 and 13 in Table 1). The die temperature was between 400–420 °C for these two trials. Figure 9b shows the surface appearance of these trials. The extrusion fabricated at 12.2 m/min exhibited a smooth surface while 13.9 m/min experienced surface tearing. For 12.2 m/min, UTS = 528.1 ± 7.9 MPa, YS = 467.9 ± 4.3 MPa, and elongation = $13.8 \pm 1.3\%$ for the T6 condition (Trial 12). The ASM Handbook states that, “with a typical extrusion ratio of 40 to 1, exit speeds of the more difficult alloys are on the order of 0.6 to 1.2 m/min” [19]. The lower strengths compared to the ASTM standard are likely due to the extrusion temperature being too low and the typical T6 solution heat treatment schedule not being optimized for ShAPE processed material.

Figure 9a shows the extrusion speed of 7075 using ShAPE (triangles) compared with textbook and handbook literature for maximum extrusion speed, regardless of extrusion ratio, for conventional linear extrusion (circles). The range of extrusion speeds given in each reference is indicated by the error bars. With ShAPE, the extrusion speed of 12.2 m/min (Trial 12 from Table 3) is approximately 10 times faster than conventional extrusion, according to the textbook and

handbook values. Such a fast extrusion speed for 7075 is promising for bringing its cost closer to 6XXX series aluminum alloys potentially enabling its wider use in the transportation industry. In addition, faster extrusion speed is more thermally efficient which can lead to lower energy consumption during manufacturing.

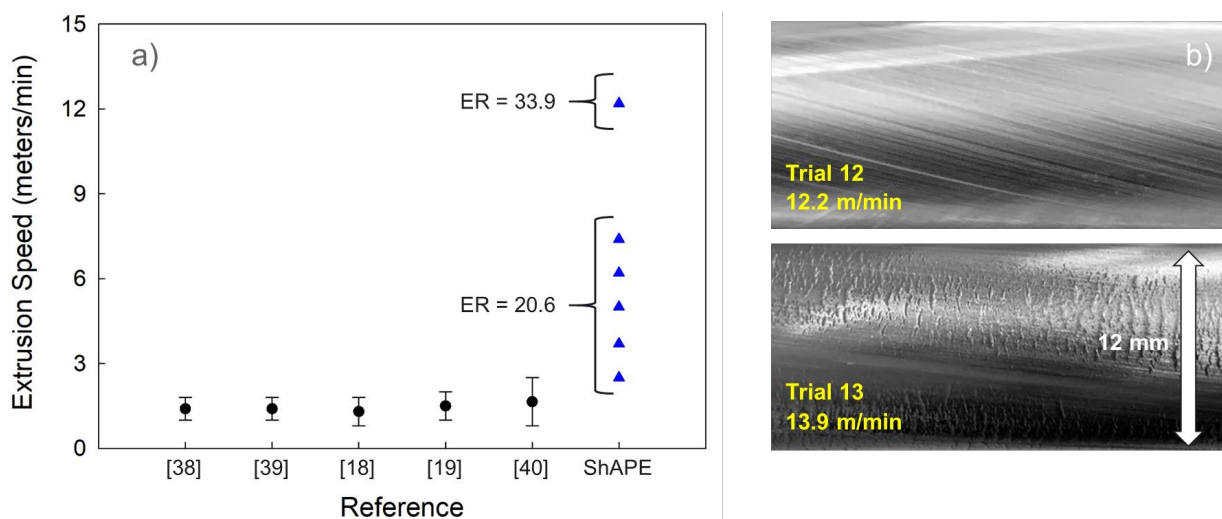


Figure 9. (a) Extrusion speed of 7075 for the ShAPE process (triangles) and conventional linear extrusion (circles). (b) 7075 tubing showing a typical surface at 12.2 m/min (ER = 33.9) and surface tearing at 13.9 m/min (ER = 40) from Trials 12 and 13 in Table 3.

Tensile data is shown in Figure 10a for extrusions fabricated at an extrusion speed of 7.4 m/min at die temperatures ranging from 341 to 441 °C is shown in Figure 10 (Trials 5–10 in Table 3). Data is not reported for Trial 11, conducted at 466 °C, due to the presence of significant surface tearing. UTS and YS were generally observed to increase as process temperature decreased. UTS ranged from a low of 530.5 ± 8.9 MPa at 441 °C (Trial 10) to a high of 565.3 ± 4.6 MPa at 362 °C (Trial 7). YS ranged from a low of 445.7 ± 6.1 MPa at 441 °C (Trial 10) to a high of 495.7 ± 8.7 MPa at 362 °C (Trial 7). These values exceed the ASTM minimum standard of 540 MPa and 485 MPa for UTS and YS, respectively [36]. In fact, UTS and YS are on par with ASM typical values of 572 MPa and 503 MPa for UTS and YS, respectively [37]. Elongation at break ranged from a low of $13.9\% \pm 1.5\%$ at 419 °C to a high of $16.8 \pm 0.8\%$ at 341 °C which exceeds the 7% ASTM minimum standard [36] and 11% ASM typical values [37]. Surface tearing was observed at 466 °C most likely due to incipient melting of LMP phases (Figure 10b). The mechanical properties for Trials 1, 5, 6, and 10 are compared with the ASTM and ASM properties in Table 4. Results for Trial 7 are also shown since this trial generally represents the highest performing extrusion.

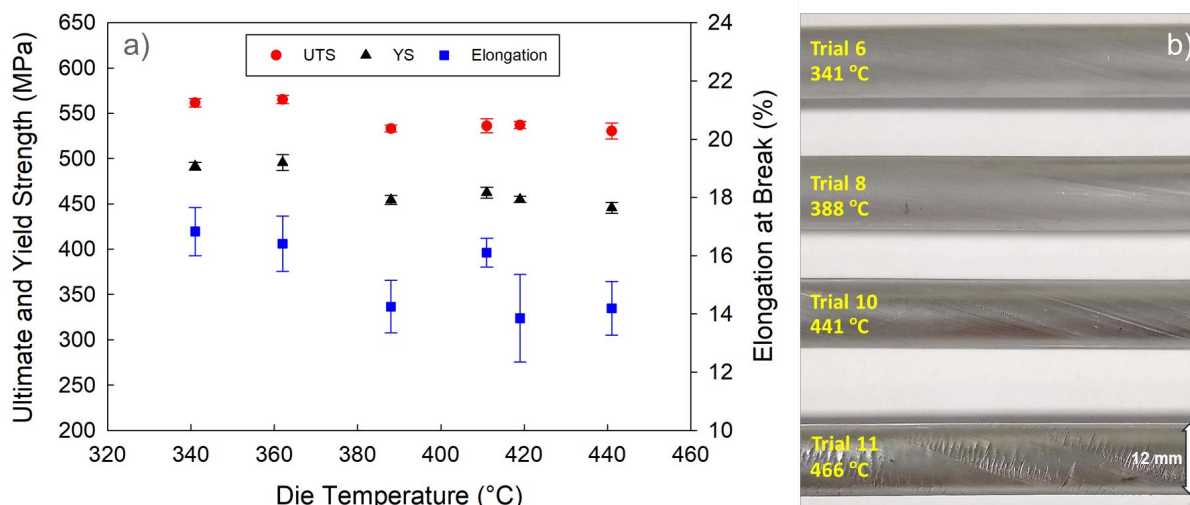


Figure 10. Figure 4. (a) UTS and YS for 7075 tubing fabricated at different die temperatures with extrusion speed held constant at 7.4 m/min (Trials 5–10 in Table 1). (b) Corresponding tube appearance with surface tearing observed at 466 °C.

Table 4. Summary of mechanical properties for ShAPE extrusions from homogenized billets compared to the ASTM and ASM values for conventional extrusion.

Extrusion Trial (#)	Extrusion Speed (m/min)	Die Temperature (°C)	UTS (MPa)	YS (MPa)	Elongation (%)
1	2.5	426	533.7 ± 8.1	438.9 ± 3.5	12.2 ± 1.1
5	7.4	419	537.0 ± 3.8	455.1 ± 3.4	13.9 ± 1.5
6	7.4	341	561.7 ± 4.5	491.6 ± 4.3	16.8 ± 0.8
7	7.4	362	565.3 ± 4.6	495.7 ± 8.7	16.4 ± 1.0
10	7.4	441	530.5 ± 8.9	445.7 ± 6.1	14.2 ± 0.9
ASTM	~1-2	~450	540	485	7
ASM	~1-2	~450	572	503	11

4.1.2 Microstructural Characterization

Microstructural evaluation was performed after ShAPE processing to understand the impact of extrusion rate and temperature. The SEM images shown in Figure 11 highlight macroscale second phase distributions that result from the extremes in speed and temperature investigated in Table 3. Results from the T6 heat-treated condition are compared with the as-extruded condition. Despite the broad range in speed and temperature, the macroscale second phase size and distribution were similar after ShAPE processing, both in the as extruded and T6 conditions. T6 heat treatment led to a significant decrease in the volume fraction of observed second phase particles at the length scale shown and weak compositional contrast aligned in the extrusion direction.

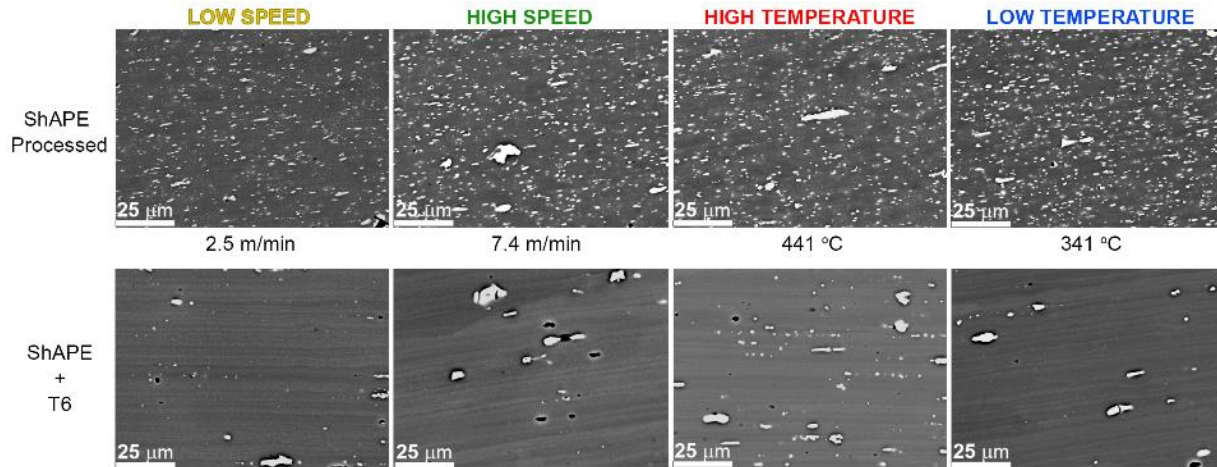


Figure 11. SEM EDS was used to identify the larger precipitates that were solutionized after heat treatment. Compositional information from the 2.5 m/min low speed extrusion is presented in Figure 6 to illustrate the effects of heat treatment further. Considerable dissolution of LMP AlMgCuZn-rich second phases is evident when single element maps are compared before (ShAPE Processed) and after heat treatment (ShAPE + T6).

EBSD was then used to evaluate grain size in the as extruded and T6 conditions. Substantial grain growth was noted following T6 heat treatment for all trials. Figure 12 shows the inverse pole figure maps highlighting grain size and texture for the 2.5 m/min extrusion in the ShAPE processed condition, an equiaxed grain size with a nominal grain diameter of ~2 μm was produced. This microstructure has undergone dynamic recrystallization because of extreme deformation during ShAPE processing. After T6 heat treatment, considerable grain growth was observed that resulted in grain elongation parallel to the extrusion direction. The grain size after heat treatment is on the order of millimeters. The reported feret diameter is shown for illustrative purposes only because most of the observed grains terminate outside the shown field of view.

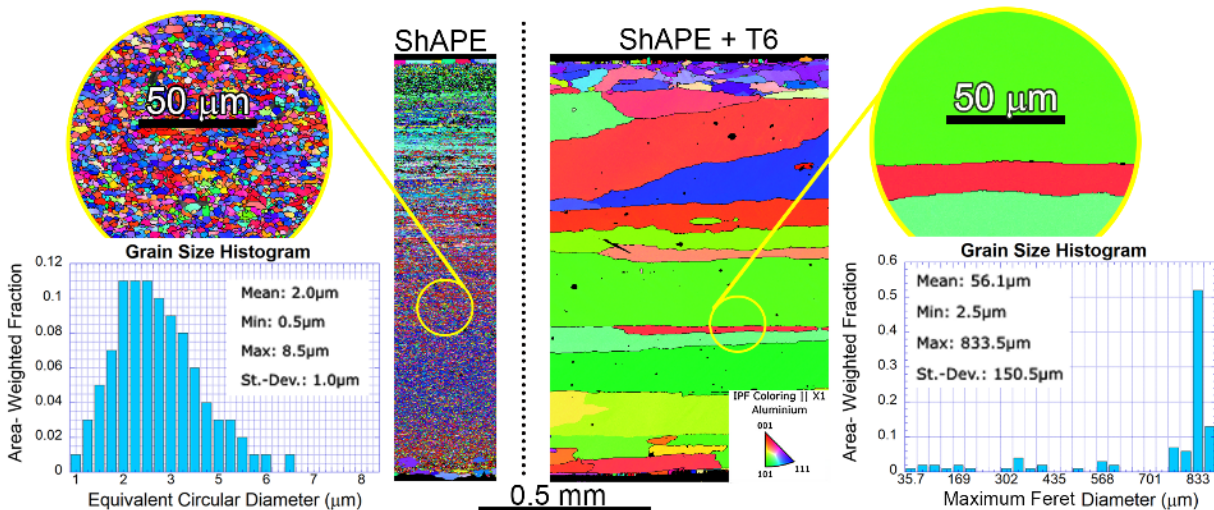


Figure 12. EBSD inverse pole figure maps from longitudinal tube cross sections show considerable grain growth following T6 heat treatment.

Disorientation angle distribution plots were generated from the entire tube wall thicknesses for the extrusions shown in Figure 11. Figure 13 shows that ShAPE processed materials exhibit a high fraction of low angle disorientation which implies extensive strain/dynamic recrystallization. The most significant deformation was observed at low temperature (341 °C). The least residual strain/low was observed in the low extrusion speed of 2.5 m/min. Disorientation distribution plots are superimposed with Mackenzie distribution [41] or random texture boundary distribution in Figure 13. T6 heat treatment resulted in grain growth that reshaped the disorientation angle plots via elimination of low angle grain boundaries, such that the resultant heat-treated microstructure approached that of a random cubic Mackenzie distribution, which is highlighted gray in Figure 13. Higher residual strain (increased low angle disorientation) in the ShAPE processed condition appears to have increased the driving force necessary to reestablish a Mackenzie distribution after heat treatment. Additionally, it is hypothesized that the increased strain at lower temperature was responsible for more completed solutionization of second phases during extrusion leading to more complete precipitation hardening during T6 tempering. Hence, high UTS and YS for billets processed at lower temperature compared to higher temperature as observed in Figure 10,

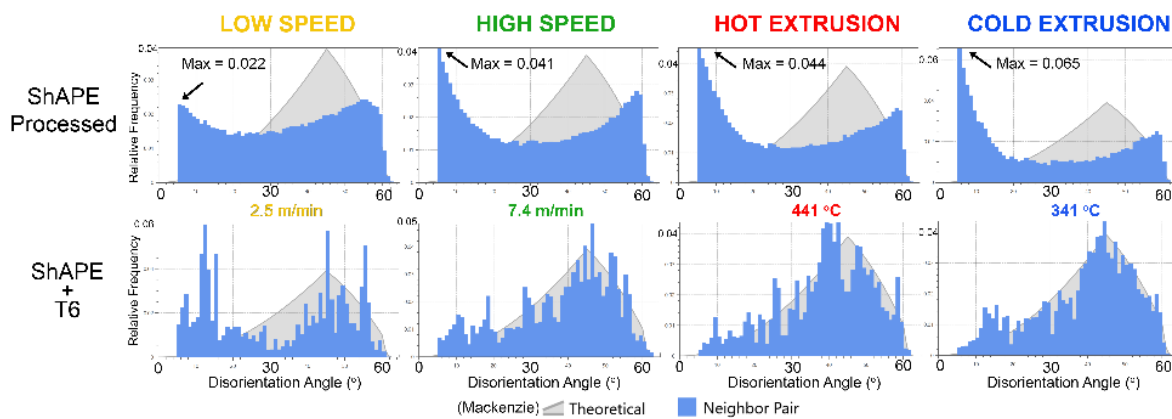


Figure 13. EBSD disorientation angle distribution plots show significant changes in the relative frequency of low angle disorientation as a function of processing condition. A typical Mackenzie distribution is shown in gray.

STEM analysis was also performed on the high and low temperature T6 extrudates to better understand the observed decrease in strength caused by the increased processing temperature on the final (T6) microstructure. Figure 14 provides a comparison of the high temperature (441 °C) and low temperature (341 °C) samples following T6 heat treatment. At lower magnification (Figures 14a and 14b) the size of the E precipitates is observed to be similar, but the density appears to be somewhat reduced in the higher temperature sample. At higher magnification, the size and density of the eta phase in the matrix (Figure 14c,d), suggests that 441 °C extrusion the hot extruded sample exhibits slightly smaller nanoscale strengthening particles than the 341 °C extrusion which are advantageous for strengthening.

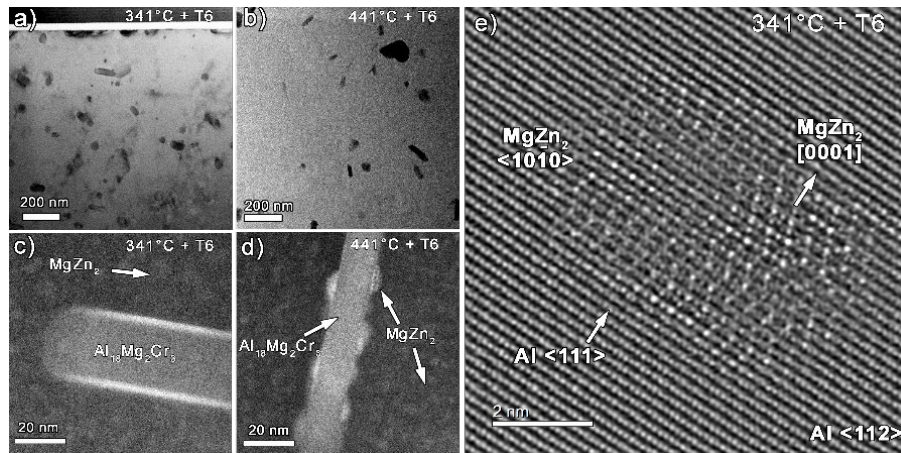


Figure 14. STEM (ADF and BF) images illustrating microstructures of the T6 heat-treated alloys following extrusion at low (341 °C) vs. high (441 °C) temperature. a,b) STEM (BF) images showing the density of secondary particles in the matrix for the low and high temperature extrusions, respectively. (c,d) STEM (ADF) images comparing the approximate dimensions of the GP zones as well as the coverage of the eta phase ($MgZn_2$) on the $Al_{18}Mg_2Cr_3$ precipitates. (e) high angle annular dark field (filtered) atomic column image showing the relative orientation of the eta phase to the Al matrix in the 341 °C heat treatment exhibiting the orientation relationship $(0001)_\eta // (111)_{Al}$ and $\langle 10-10 \rangle_\eta // \langle 112 \rangle_{Al}$.

Table 5. TEM findings 341 °C and 441 °C process temperature comparison in the T6 condition.

	$Al_{18}Mg_2Cr_3$ precipitates (E phase)	$MgZn_2$ (η , Eta Phase)
341 °C	High Density	Larger
441 °C	Low Density	Smaller

The key observations and conclusions from the work on homogenized 7075 billets are as follows.

- ShAPE extrusion of homogenized 7075 billets reached extrusion speeds of up to 12.2 m/min without tearing which is up to 10 times faster than is possible with conventional linear extrusion.
- ShAPE processed 7075 in the T6 condition achieved UTS = 565.3 ± 4.6 MPa and YS = 495.7 ± 8.7 MPa, which exceed the ASTM minimum standard and are on par with ASM typical values. Elongation = $16.8 \pm 0.8\%$ was significantly higher than the ASTM (7%) and ASM (11%) values.
- T6 heat treatment of ShAPE processed samples leads to considerable grain growth (mm scale) where significant elongation is observed parallel to the extrusion direction.
- Low temperature extrusion gave superior mechanical performance compared to high temperature extrusion which arose from differences in nanoscale second phase distributions.

4.2 ShAPE Extrusion of 7075 Unhomogenized Billets

4.2.1 Mechanical Testing

Due to the extensive grain, and second phase, refinement observed during ShAPE extrusion of homogenized billet, we turned to exploring the possibility of using unhomogenized billets. If successful, this would eliminate the thermally intensive homogenization heat treatment that is approximately 20 hours at 430 °C. It was hypothesized that the extreme deformation at elevated temperature inherent to ShAPE could perform the homogenization heat treatment in situ during the extrusion process. To that end, a series of experiments was carried out as shown in Table 6.

Table 6. Process parameters for ShAPE extrusion of 7075 unhomogenized billets.

Extrusion Trial (#)	Ram Speed (m/min)	Extrusion Ratio	Extrusion Speed (m/min)	Rotation Speed (rpm)	Die Temperature (°C)
1	0.12	20.6	2.5	50	429
2	0.18	20.6	3.7	50	393
3	0.18	20.6	3.7	40	378
4	0.18	20.6	3.7	30	359
5	0.18	20.6	3.7	24	337
6	0.30	20.6	6.2	36	358
7	0.36	20.6	7.4	50	374

Mechanical test results for the trials in Table 6 are shown in Table 7 for ShAPE tubing heat treated to the T6 condition. The experimental results are compared with the ASTM and ASM standard for T6 material made by conventional extrusion of homogenized billets. It was observed mechanical properties were highest when billets were processed at lower temperature. Trial 6 is particularly noteworthy where UTS = 591.31 ± 3.5 MPa, YS = 530.8 ± 2.3 MPa, and elongation = $16.0 \pm 0.8\%$ for the T6 condition substantially exceeded the ASTM and ASM standards. This is remarkable given that unhomogenized billets are generally considered to be un-extrudable. As such, the energy intensive homogenization step can be eliminated by ShAPE (in addition to billet pre-heating) while also extruding at 6.2 m/min compared to 1-2 m/min for conventional extrusion for 7075, all while achieving exceptional mechanical properties.

Table 7. Summary of mechanical properties for ShAPE extrusions from unhomogenized billets compared to the ASTM and ASM values for conventional extrusion.

Extrusion Trial (#)	Extrusion Speed (m/min)	Die Temperature (°C)	UTS (MPa)	YS (MPa)	Elongation (%)
1	2.5	429	528.3 ± 4.6	435.9 ± 7.4	15.7 ± 0.9
2	3.7	393	538.3 ± 2.5	457.7 ± 5.0	14.7 ± 0.8
3	3.7	378	586.3 ± 9.2	517.0 ± 6.7	16.1 ± 0.7
4	3.7	359	596.2 ± 4.7	531.0 ± 3.0	17.4 ± 0.3
5	3.7	337	575.4 ± 3.0	506.5 ± 2.2	17.0 ± 0.6
6	6.2	358	591.3 ± 3.5	530.8 ± 2.3	16.0 ± 0.8
7	7.4	374	Surface tearing and cracking		
ASTM	~1-2	~450	540	485	7
ASM	~1-2	~450	572	503	11

4.2.2 Microstructural Characterization

EBSD analysis was conducted using SEM with a scanning area of $\sim 200 \mu\text{m} \times 250 \mu\text{m}$ on locations (a)-(e) shown in the optical image of Figure 15. Additionally, secondary electron (SE) images were used to reveal the evolution of the secondary phases. The very early stage of deformation due to ShAPE is shown in Figure 15(e). Coarse grains surrounded by high angle grain boundaries (HAGBs) can be observed by the band contrast (BC) and inverse pole figure (IPF) images. Kernel average misorientation (KAM) analysis shows incipient strain accumulation around intragranular and interdendritic secondary phases. As shown in the SE image in Fig. 15(e), the intragranular acicular secondary phase is highlighted with a dashed red arrow, while the grain-boundary secondary phase is highlighted with a continuous red arrow.

At transition zone I, shown in Figure 15(d), grain fragmentation is observed by the formation of low angle grain boundaries (LAGBs), depicted as yellow lines in the BC figure. The IPF image shows the development of a small intragranular rotation, which is more clearly highlighted by the KAM analysis. The presence of secondary phases intensifies intragranular misorientation accumulation. Simultaneously, grain-boundary secondary phases (black arrows in the SE image), undergo partial fracture and dissolution.

As strain and temperature further increase within transition zone II (Figure 15(c)), three important phenomena can be differentiated: grain stretching, secondary phase dissolution, and dynamic recrystallization. First, the BC and IPF images show the presence of stretching Al grains due to the extrusion process. Discontinuous dynamic recrystallization (DDRX) occurs at dendritic interfaces (dashed circles) and at previous grain boundaries (solid circles), as detailed by the IPF map. KAM analysis indicates that these new grains are mostly strain-free, while strain accumulation occurs at the interior of the extruding grains. Finally, a more advanced stage of the dissolution of the thick grain boundary and acicular intragranular phases simultaneously occurs, while only spherical intragranular secondary phases are still observable in the SE image.

The processed zone (Figure 15(b)) consists of high-density refined Al grains oriented in the extrusion direction. The IPF image clarifies that these are independent grains with nearly randomized crystal orientations, typically observed during the activation of geometric dynamic recrystallization (GDRX). KAM analysis indicates the strong reduction in the intragranular misorientation during GDRX, whereas SE analysis indicates additional secondary phase dissolution, where only some coarse secondary phase particles remain oriented in the extrusion direction. The microstructure within the extruded tube is displayed in Figure 15(a). Strong grain refinement is also observed, similar to that in the processed zone. However, these grains do not show preferential extrusion alignment. Additional reduction in the intragranular misorientation and in the density of secondary phases can be seen simultaneously in the KAM analysis and SE images. The evolution of the misorientation distribution histograms from the base metal to the extruded microstructure is shown in Figure 16. Locations (a) and (b) show strong dynamic recrystallization due to the high frequency of HAGBs and the relatively small frequency of LAGBs. Locations (c) and (d) predominantly show grain fragmentation due to the high frequency of LAGBs caused by strain accumulation. Finally, location (e) shows the coarse-grained as-cast base material microstructure with little if any LAGBs.

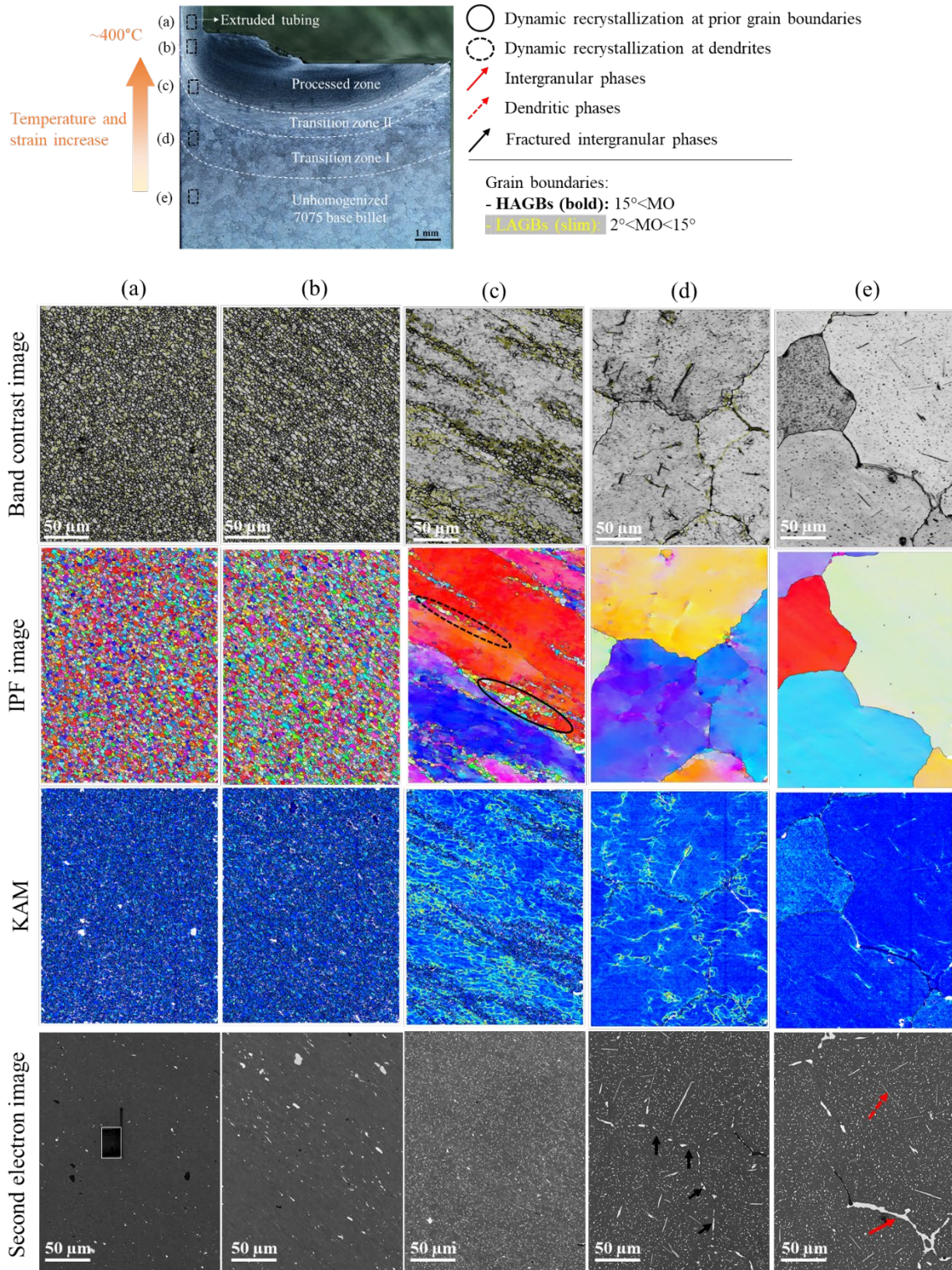


Figure 15. Optical image displaying five distinct regions from top to bottom: (a) extruded microstructure, (b) processed zone, (c) transition zone II, (d) transition zone I, and (e) unhomogenized 7075 Al alloy base; EBSD analysis and SE images of selection regions (a)-(e).

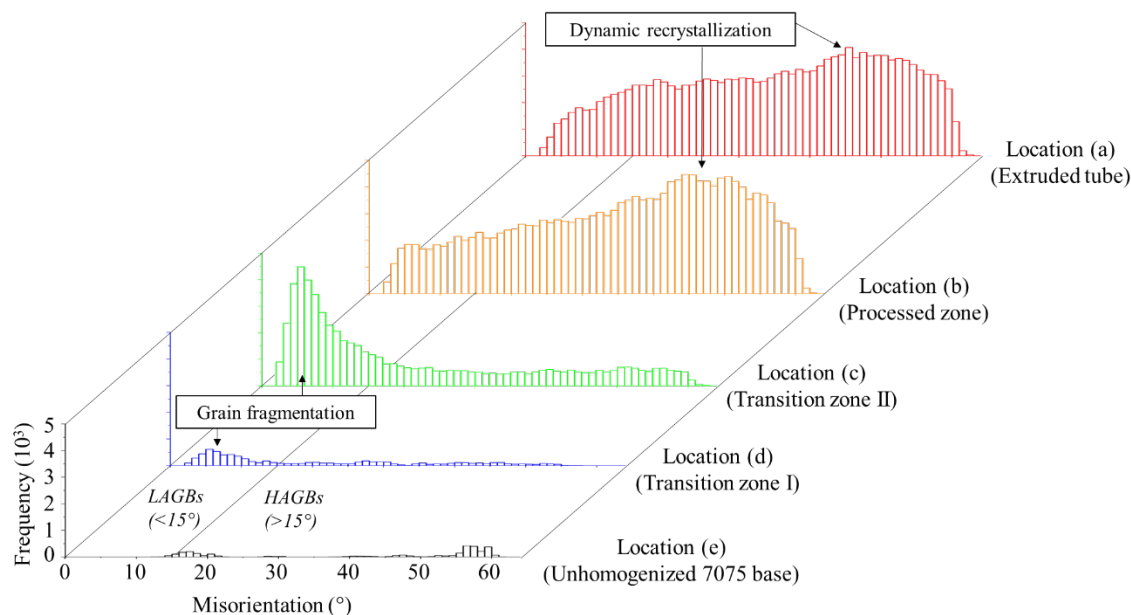


Figure 16. Evolution of the misorientation distribution histograms throughout the microstructural regions of interest. These correspond to the locations labeled in Figure 15 as (a)-(e).

TEM was applied to further reveal the mechanism of local microstructure evolution. As displayed in the BF-TEM images (Figure 17(a)), the width of grain refining region is $\sim 5 \mu\text{m}$ (marked with yellow dash lines). Based on the dark-field (DF) TEM images from selected regions (Figure 17(b) and (c)), secondary phases are consumed by intragranular and grain-boundary diffusion. This can be attributed to the eutectic reaction between the Al matrix and second phases of MgZnCu. Cu first diffused out of secondary phases during plastic deformation of the unhomogenized 7075 Al alloy, as shown in Figure 18. Meanwhile, the alloying elements in the matrix of the grain refining region (labeled in Figure 18) are compared with the base material, and increasing Cu, Mg, and Zn is observed, as shown in the plot of Figure 19.

The difference in secondary phases between the base region and the processed zone were further investigated using TEM. With redissolution of Cu from the MgZnCu-enriched phase, not only the configuration changed significantly from the initial spindle to irregular morphology (Figure 20(a) and (e)), but the crystal structure also evolved from single crystal into polycrystal (Figure 20(b) and (f)). In addition, another nanoprecipitate (i.e., E-phase ($\text{Al}_{18}\text{Mg}_3\text{Cr}_2$)), often detected in 7075, also varied from the initial crystal structure to amorphous due to severe plastic deformation (Figure 20(c) and (g)). Notably, GP zones, η' , and η precipitates were not detected in the Al matrix in the base region and the processed zone (Figure 20(d) and (h)). Meanwhile, elemental distribution of the secondary phases shown in Figure 20(a) and (e) are shown in Fig. 21, and a clear trend of redistribution in Mg, Zn, and Cu can be observed.

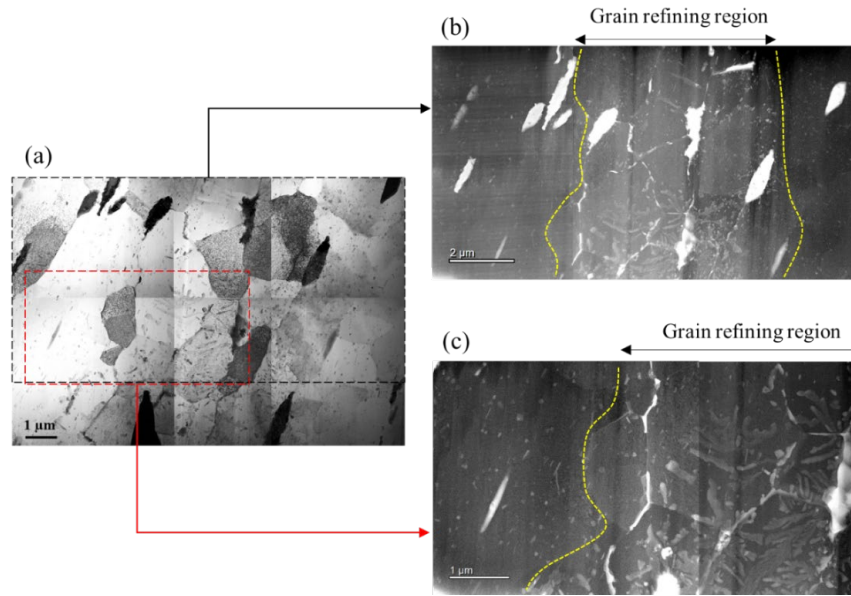


Figure 17. (a) BF- and (b,c) DF-TEM images of the grain-refinement region (location (c) labeled in Figure 15).

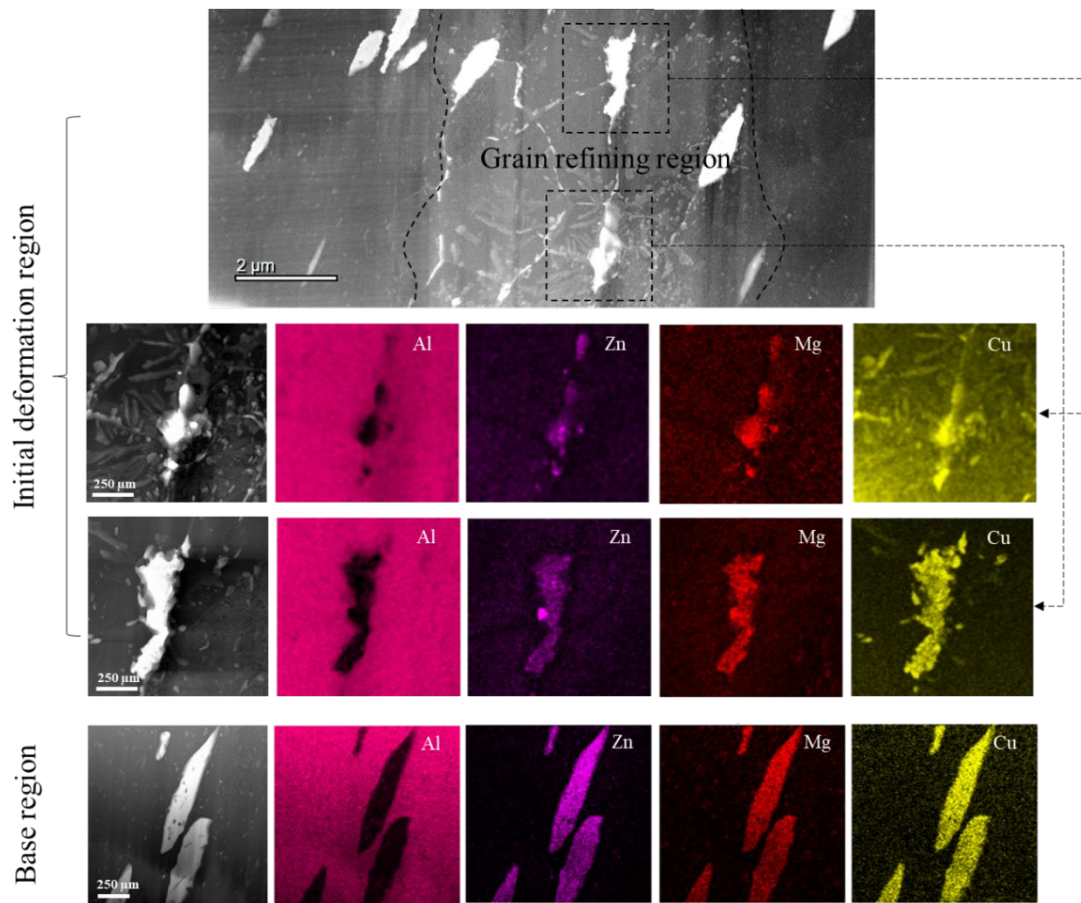


Figure 18. DF-TEM and EDS map of Al matrix and main alloying elements of Zn, Mg and Cu in grain refining region and base 7075.

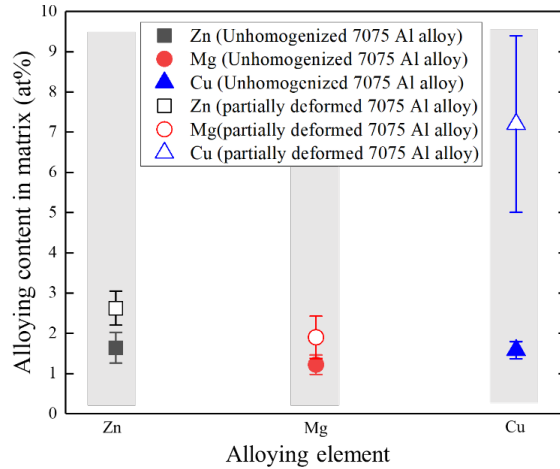


Figure 19. Comparison of the alloying elements in the matrix between the unhomogenized base and the grain-refined region.

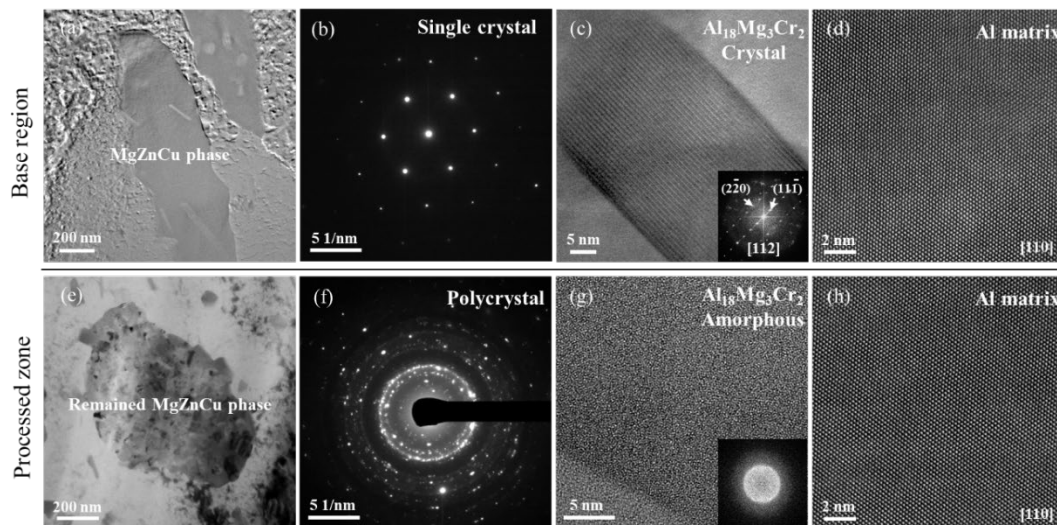


Figure 20. Secondary phase variation during deformation. (a) and (e) BF-TEM images showing the initial spindle and the deformed irregular morphology of MgZnCu particles in the base region and the processed zone, respectively. (b) and (f) SAED patterns showing the single crystalline and polycrystalline structures of the MgZnCu phases in (a) and (e), respectively. (c) and (g) High-Resolution TEM image showing the crystalline and amorphous structures of the E phases, respectively. (d) and (h) HAADF-STEM images of the Al matrix.

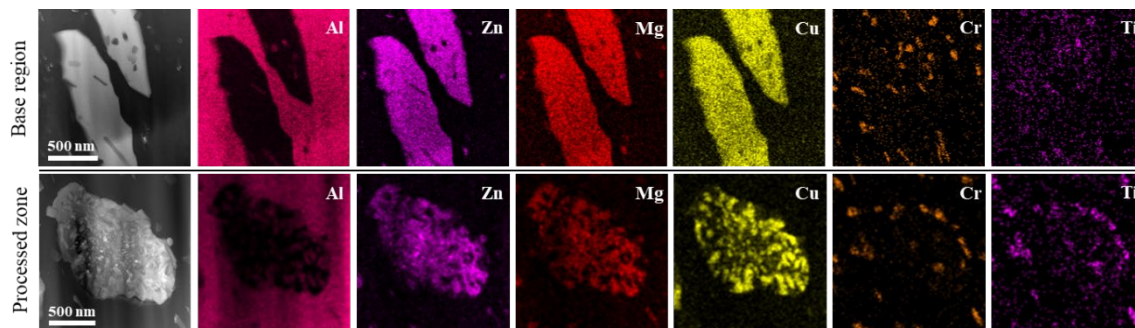


Figure 21. TEM-EDS mapping of the particles in Figure 20(a) and (e).

The key observations and conclusions from the work on unhomogenized 7075 billets are as follows.

- The extrusion speed of 6.2 m/min for unhomogenized 7075 billets by ShAPE exceeds the 1–2 m/min ceiling for conventional extrusion of homogenized 7075 billets.
- The thermally intensive homogenization step required for conventional extrusion of 7075 is eliminated using the ShAPE process. Billet pre-heating in a separate furnace was also eliminated.
- Enhanced extrudability in unhomogenized 7075 via ShAPE results from strain-accelerated thermomechanical dissolution and/or fracture of deleterious interdendritic phases.
- Extreme grain refinement is achieved by the substructure-to-LAGBs-to-HAGBs transformation sequence via discontinuous dynamic recrystallization and geometric dynamic recrystallization during ShAPE.
- The mechanical properties of ShAPE tubing made from unhomogenized casting and then heat treated to the T6 condition were as high as UTS = 596 ± 4.7 MPa, YS = 530 ± 3.0 MPa, and Elongation = 17.4 ± 0.34 % elongation for Trial 4 which substantially exceed the ASTM standard values for conventional extrusion of homogenized 7075 billet.

4.3 ShAPE Extrusion of 7075 with Quenching

It was hypothesized that the high extrusion speeds obtained during ShAPE extrusion of 7075 could enable press quenching (the act of combining extrusion with solution heat treating), thereby eliminating the need for solution heat treating prior to artificial aging. Elimination of solution heat treating would bypass yet another thermal treatment step typical of conventionally extruded 7075, further reducing the embedded energy of ShAPE extrusions. To that end, extrusions carried out on homogenized and unhomogenized billets with the water quench system active as show in Table 8. Typical T6 heat treatment is 24 hr at 120 °C for the artificial aging step and times of 12 and 48 hours were also investigated to see if a shorter artificial aging time might also be enabled by ShAPE.

Table 8. Parameters for ShAPE extrusion of 7075 homogenized and unhomogenized billets.

Extrusion Trial (#)	Feedstock	Artificial Aging	Extrusion Speed (m/min)	Extrusion Ratio	Rotation Speed (rpm)	Die Temperature (°C)
1	Homogenized	12 hr at 120 °C	7.4	20.6	30	400
		24 hr at 120 °C				
		48 hr at 120 °C				
2	Unhomogenized	12 hr at 120 °C	3.7	20.6	30	380
		24 hr at 120 °C				
		48 hr at 120 °C				

Table 9 shows tensile test results for ShAPE extruded 7075, from homogenized and unhomogenized billets, that underwent artificial aging without solution heat treating, which essentially a T5 temper. These results are compared against T6 properties for conventionally extruded 7075. In Table 9, it is observed that unhomogenized billets did not exhibit precipitation hardening as evident by the low ultimate and yield strengths. This is likely due to high melting point second phases in the unhomogenized ingots not going into solution during extrusion. However, homogenized billet exhibited a strong age hardening response as evident by the UTS and YS being on par with conventionally extruded homogenized billets in the T6 temper. Microstructural characterization to explain the mechanism was not performed due to the lateness in the project of this discovery but is ripe for publication.

Table 9. Tensile properties of ShAPE extruded 7075, from homogenized and unhomogenized billets that underwent artificial aging without solution heat treating first.

Extrusion Trial (#)	Feedstock	Artificial Aging	UTS (MPa)	YS (MPa)	Elongation (%)
1	Homogenized	12 hr at 120 °C	573 ± 4.1	517 ± 4.3	13.1 ± 1.4
		24 hr at 120 °C	588 ± 0.7	535 ± 1.7	14.8 ± 0.9
		48 hr at 120 °C	578 ± 4.9	526 ± 5.5	13.8 ± 1.8
2	Unhomogenized	12 hr at 120 °C	330	235	14.5
		24 hr at 120 °C	330	237	14.6
		48 hr at 120 °C	319	233	15.5
ASTM (T6)	Homogenized	24 hr at 120 °C	540	485	7
ASM (T6)	Homogenized	24 hr at 120 °C	572	503	11

The key conclusion from the work on quenched 7075 is as follows.

- Press quenching of 7075 was achieved for ShAPE extruded material. T6 properties were achieved with a T5 temper.

4.4 ShAPE Extrusion of 2024

4.4.1 Mechanical Testing

Based on the success of 7075, a brief study was performed in 2024 to determine if fast extrusion speeds could also be achieved and if materials properties could likewise be improved. Given that 2024 is the most widely used of all aerospace alloys, the potential for reduced energy and cost in manufacturing while improving material properties could be extremely impactful. To that end, a series of experiments was carried out as shown in Table 10 with the control variables being ram speed and rotational speed, and the response variables being ram force and die temperature as measured. Ram pressure is calculated based on the ram force and billet area of 7.13 cm². Die rotational speeds were selected to impose a range of temperatures. From the friction stir welding literature for 2024-T351, it is known that nugget hardness increases with process temperature and peaks above 450 °C due to more complete solutionizing of alloying elements (i.e. more dissolving of S phases) [42,43]. For this reason, a range of temperatures from approximately 460-500 °C were examined to find the process temperature that gives peak strength for ShAPE extruded 2024 tubes. As a screening method to find the optimum process temperature, tubes fabricated per Table 2 were heat treated to the T6 condition to avoid the complication of cold working required for T3510 and T8510. T6 tempering involved solution heat treating at 495 °C for 1 hr, water quenching, and artificial aging at 190 °C for 10 hrs.

Table 10. Process parameters for ShAPE extrusion of 2024-T351 billets.

Extrusion Trial (#)	Ram Speed (m/min)	Extrusion Ratio	Extrusion Speed (m/min)	Rotation Speed (rpm)	Die Temperature (°C)	Ram Force (kN)	Ram Pressure (MPa)
1	0.36	20.6	7.4	65	461	575	807
2	0.36	20.6	7.4	75	482	540	758
3	0.36	20.6	7.4	80	495	513	721

The results section will show that the highest strengths were achieved for Trial 2. The process conditions of Trial 2 were replicated for additional extrusions which were then tempered to the T3510 and T8510 conditions and are the primary focus of this work. Cold working for these tempers is accomplished by stretching a 60 cm length of the tube on an MTS 22 kN servo hydraulic test frame to 3.5% and 4.5% strain. A displacement rate from the upper grip and 20 mm from lower grip. Stretching proceeded until either of the two extensometers reached the target strain value.

Figures 22(a) and (b) present the extrusion ram force and die temperature as a function of extruded tube length for the trials listed in Table 10. These process data were captured for a representative extrusion length of 800 mm at an extrusion speed of 7.4 m/min. It is observed in Figures 22 (a-b) that the ram force and die temperature reaches near steady-state for Trials 1 and 2. However, in Trial 3, the ram force started low (about 200 kN) while the die temperature was above 510 °C. Ram force increased as temperature decreased below 500 °C by adjusting the rotational speed to 80 RPM (Table 10). The surface appearance of the tubes extruded at different die temperatures are illustrated in Figure 22 (c). Trials 1 and 2 reveal good quality tube with smooth surfaces which are free from defects such as scoring or tearing (see Figure 22-c). With increasing die temperature, the surface appearance tends to change from a smooth

surface at 495 °C to a cracked surface at 510 °C (Figure 22-c). Therefore, no characterization was conducted for the tubes produced above 495 °C.

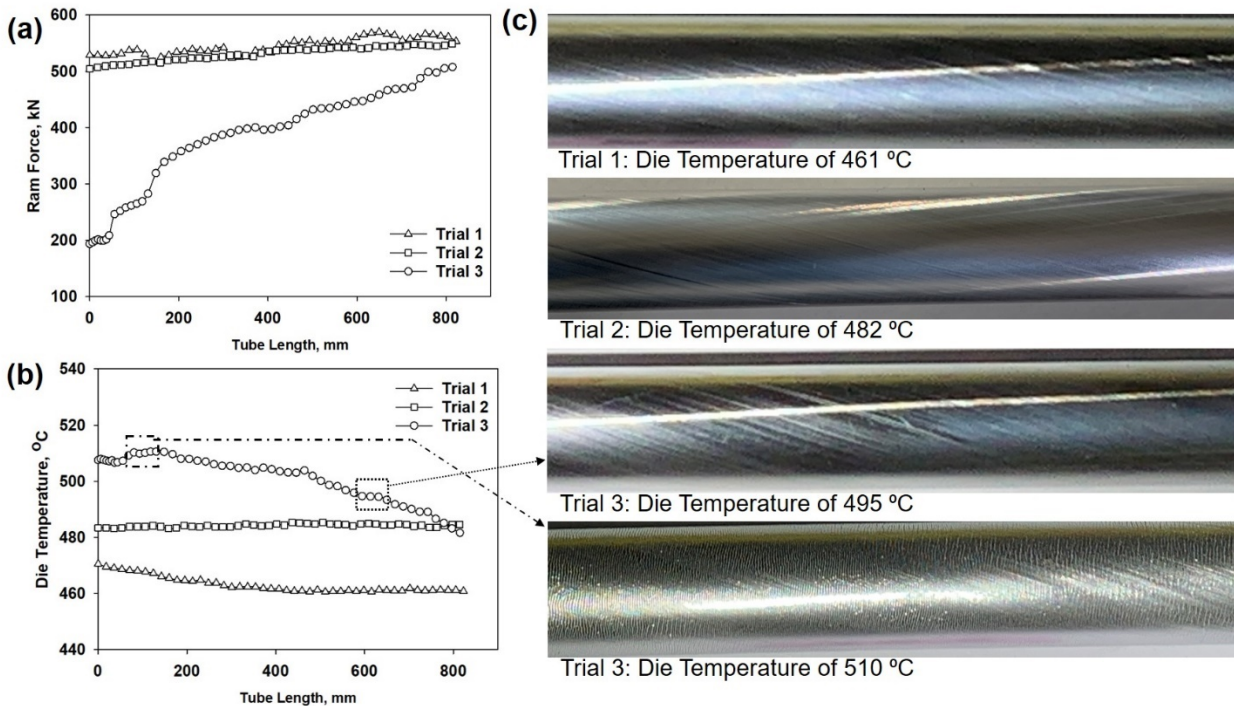


Figure 22. (a) Extrusion ram force and (b) die temperature, and (c) surface appearance of ShAPE extruded tubes at different die temperature.

The tensile stress-strain curves of the 2024 tubes from Trials 1-3, heat treated to the T6 condition along with as received 2024-T351 precursor material, are shown in Figure 23. The ultimate tensile strength (UTS), 0.2% yield strength (YS), and % elongation at break are presented in the inset table of Figure 23. The highest UTS and YS are observed in Trial 2 which has a die temperature of 482 °C while the % elongation at break decreases with increasing process temperature. These UTS and % elongation of Trial 2 are similar to those of as received 2024-T351 precursor materials, however the YS of ShAPE + T6 was compromised which indicates the importance of cold work in improving the YS of 2xxx series Al alloys. As discussed in the experimental section, this T6 condition was studied to determine the optimum extrusion temperature for subsequent investigation of T3510 and T8510 tempers. Therefore, Trial 2 was replicated and T3510 and T8510 heat treatment conditions were applied to further explore the mechanical properties of ShAPE extruded 2024 tubes.

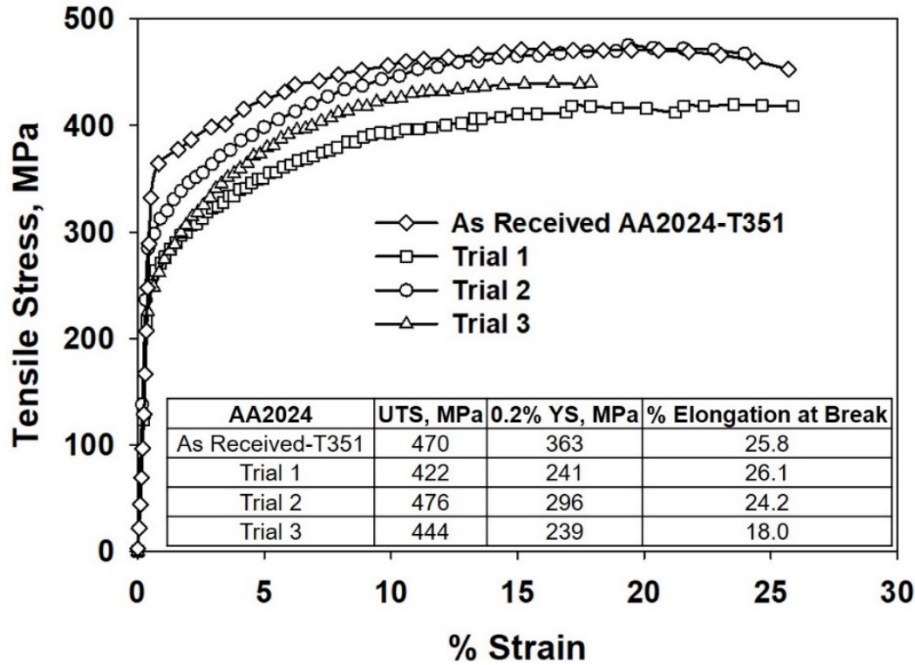


Figure 23. Stress-strain curves of as received 2024-T351 precursor and ShAPE extruded 2024-T6 tube.

Figure 24 compares the tensile stress-strain curves of representative ShAPE extruded 2024 tubes after different post extrusion heat treatment. A significant increase in the YS is observed in T3510 and T8510 tempered tubes as compared to T6 condition because of the effect of cold working [44, 45].

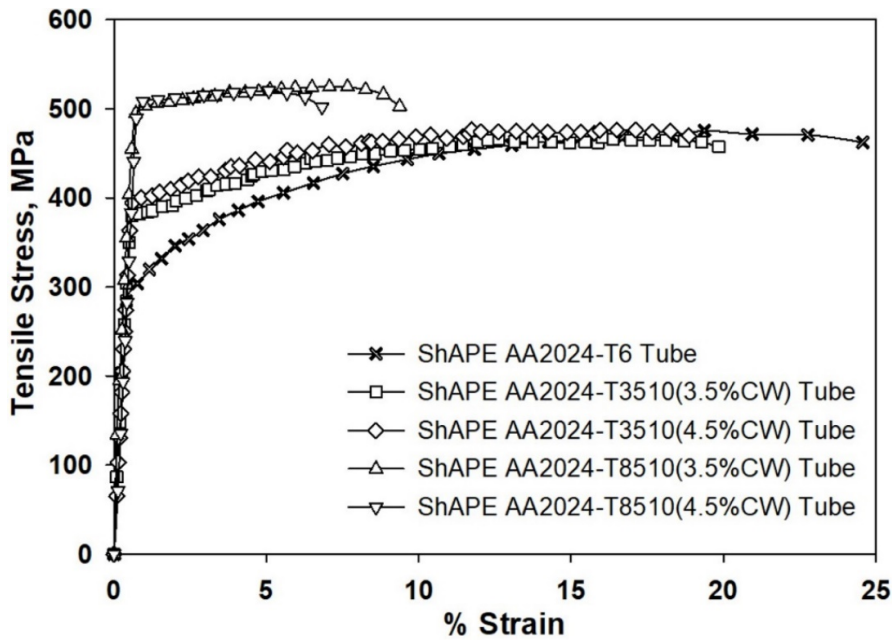


Figure 24. Stress-strain curves of 2024 tube after different post extrusion tempering including T6, T3510 and T8510.

Figure 25 (a-c) graphically illustrate the comparison of the UTS, 0.2% YS and % elongation at break of the AA2024 ShAPE tubes after the application of different tempers with respect to those of standard and industry values. The YS of 2024 ShAPE tubes exceeded the ASTM minimum, ASM typical (indicated dashed horizontal lines in Figure 25 (a-c)) and maximum reported industrial values (dotted horizontal lines in Figure 25 (a-c)) [44, 46, 47]. In Addition, the UTS and elongation of ShAPE extruded tubes with respective tempers are also improved compared to ASTM minimum and ASM typical values and are on the par with industry reported values. In essence, with T8510 treatment (3.5 → 4.5% cold working), the UTS and YS of tubes were improved by 18% and 32% respectively from the ASM-typical and ASTM minimum values.

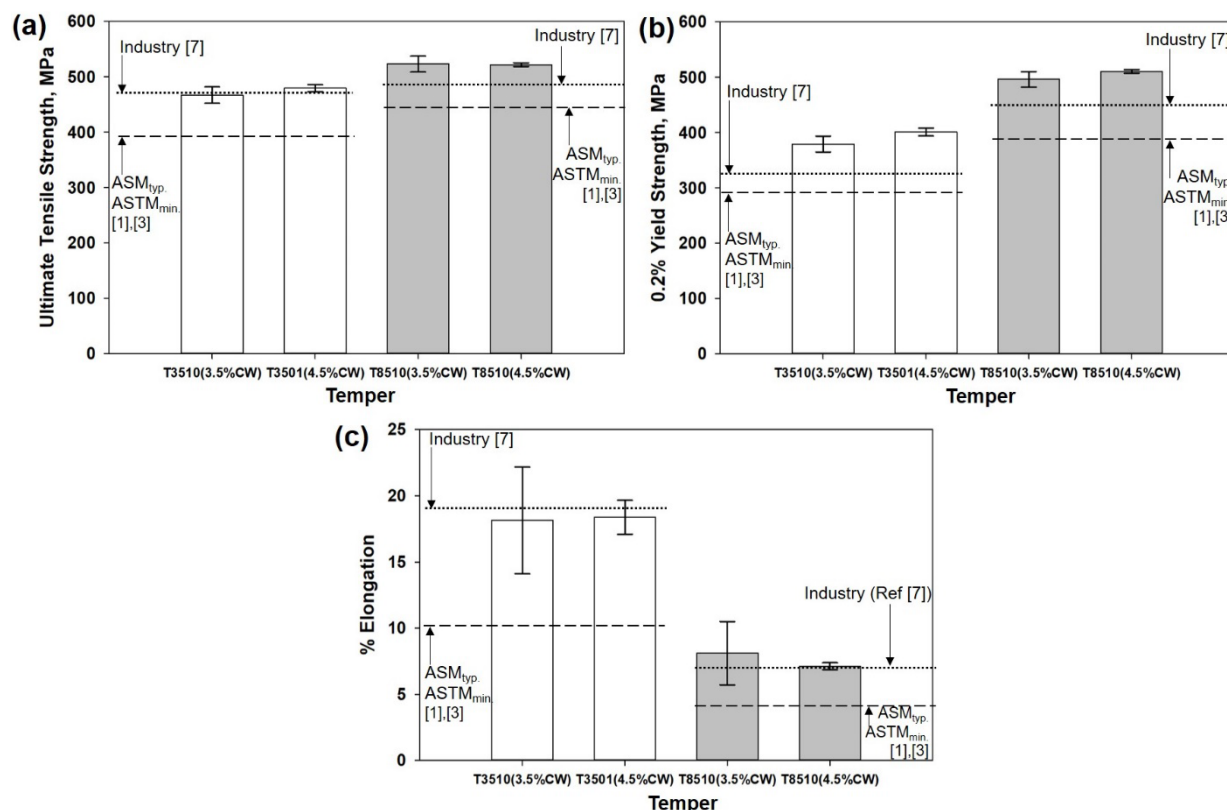


Figure 25. Comparison of tensile properties of different tempered 2024 ShAPE extruded tubes and relevant standard values: (a) ultimate tensile strength, (b) 0.2% yield strength, and (c) % elongation.

4.4.2 Microstructural Characterization

Figures 26 (a) and (d) schematically show the EBSD specimen locations in the as-received 2024-T351 extruded bar and ShAPE extruded 2024 tube in both transverse and longitudinal sections. The typical IPF maps of as-received 2024 in transverse and longitudinal sections are shown in Figure 26 (b) and (c). The as-received 2024 microstructures in Figure 26 (b) exhibited average grain size of $69.9 \pm 31.3 \mu\text{m}$. However, the as-received 2024 has elongated grains in the extrusion direction with weighted average grain size of $123.9 \pm 62.5 \mu\text{m}$ shown in Figure 26 (c). A significant grain refinement was observed after the ShAPE process as shown in Figures 26 (e) and (f) with measured grain sizes within the range 10-50 μm . The transverse section (Figure 26 (e)) possesses mostly equiaxed grain with larger grains toward the ID of the ShAPE tubes. However, the slightly elongated grain in the extrusion direction was observed in the longitudinal section (Figure 26(f)).

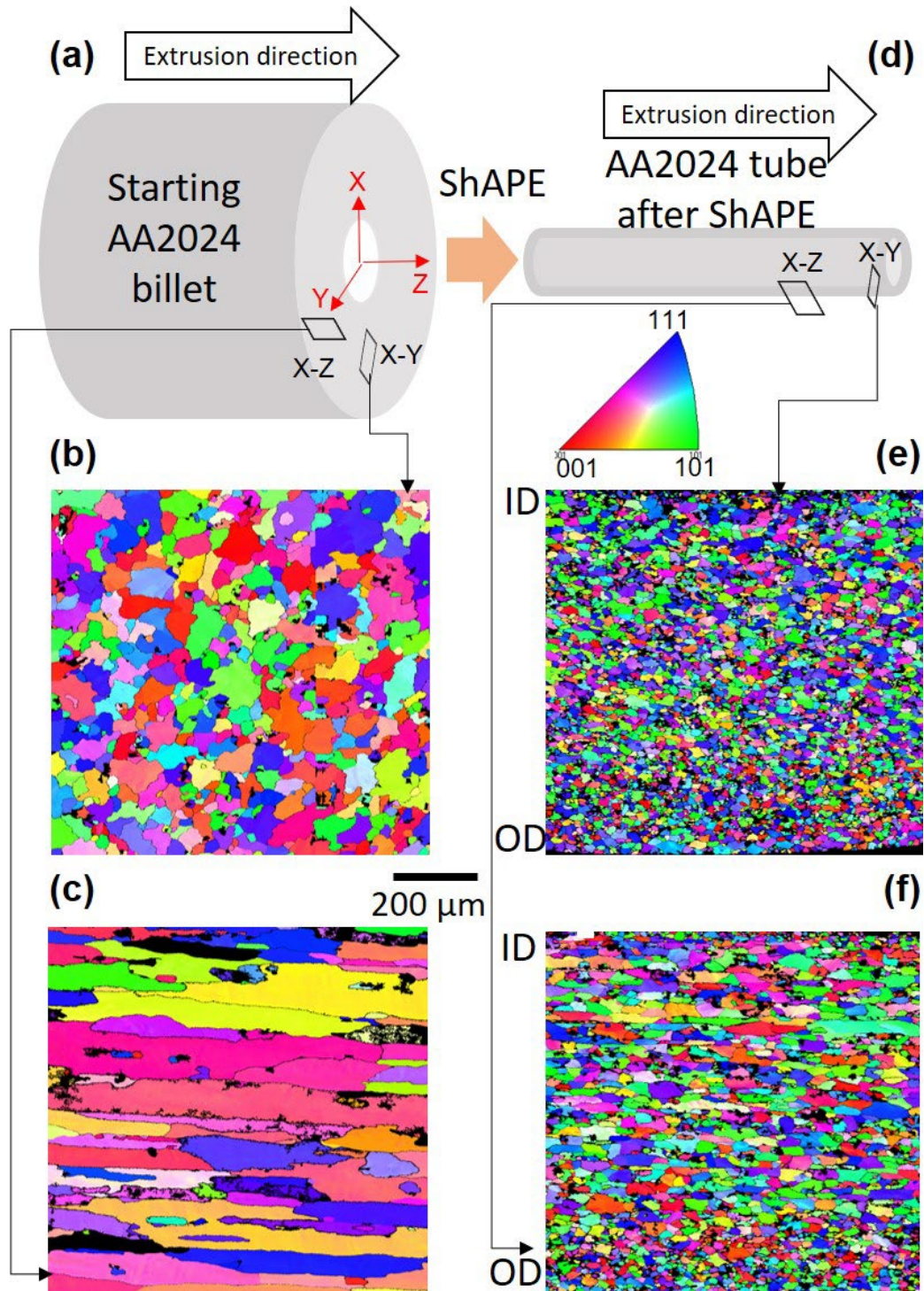


Figure 26. EBSD analyses of transverse and longitudinal microstructures of 2024: (a) As-received 2024-T351 bar with schematic orientation of transverse and longitudinal section, (b) transverse grain microstructures of as-received bar, (c) longitudinal grain microstructures as-received bar, (d) ShAPE extruded 2024 tube with schematic orientation of transverse and longitudinal section, (e) transverse grain microstructures of ShAPE extruded tube, (f) longitudinal grain, microstructures of ShAPE extruded tubes.

Figures 27 (a-h) reveals the transverse (Figures 27 (a-d)) and longitudinal (Figures 27 (e-h)) grain microstructures of ShAPE extruded 2024 tubes after different post extrusion heat treatments. Table 11 also presents the grain size measurements of ShAPE extrude tubes with different post extrusion heat treatments in corresponding sections. While the difference in grain sizes after different tempers are statistically insignificant, the artificial aging for obtaining T8510 conditions resulted in a peripheral coarse grain (PCG) [48] growth along the OD of the tube (see Figure 27 (c-d)). These coarser grain in T8510 condition also appear after few layers of finer grain from the ID of the tube and extend towards the half of the tube wall thickness (Figure 27(c)). It is also interesting to note that increasing the cold working from 3.5% to 4.5% resulted in a slight reduction in grain size for T8510 temper (Figure 27(d)). In the longitudinal section, the average grain size was reduced to $26.0 \pm 11.6 \mu\text{m}$ and $22.0 \pm 10.2 \mu\text{m}$ for naturally aged 2024 ShAPE tubes with 3.5 % (Figure 27 (e)) and 4.5 % (Figure 27(f)) cold work. However, the grain growth occurred in the artificial aging samples in the whole area of the longitudinal section resulted in an increased grain size of $32.9 \pm 17.8 \mu\text{m}$ and $26.5 \pm 12.2 \mu\text{m}$ for 3.5 % (Figure 27(g)) and 4.5 % (Figure 27(h)) cold worked tubes. Overall, the variation of grain sizes through the tube wall thickness is obviously different in longitudinal (Figure 27 (e-h)) section compared to transverse section (Figure 27 (a-d)). Nevertheless, the trend of the grain size spreading is similar in both sections such that, very fine grains in first few layers toward the ID of the tube ($< 40 \mu\text{m}$) followed by coarser near center to ID ($< 600 \mu\text{m}$), finer near center to OD ($< 300 \mu\text{m}$), and PCG at the OD ($< 80 \mu\text{m}$). In T3510 and T8510 temper with 3.5% and 4.5% cold work, grain size in the transverse and longitudinal sections of ShAPE extruded tubes are dramatically refined and equiaxed compared to the conventionally extruded T351 feedstock.

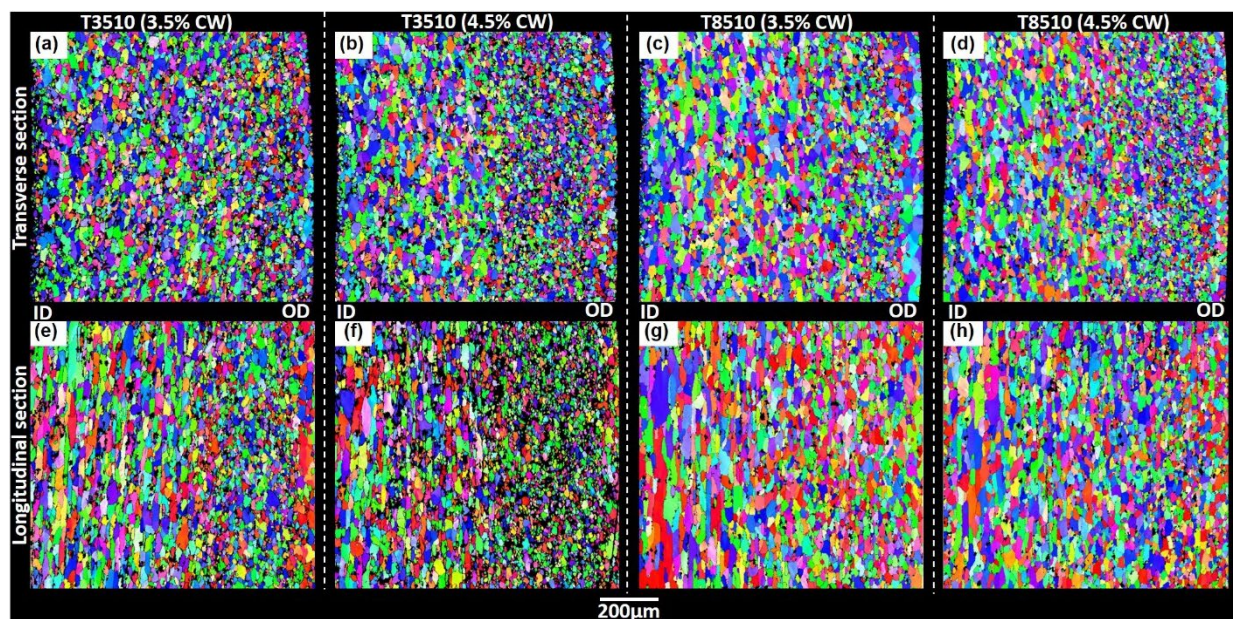


Figure 27. Grain microstructures of 2024 ShAPE extruded tubes from EBSD IPF after different post extrusion heat treatment: (a) transverse T3510 (3.5% CW), (b) transverse T3510 (4.5% CW), (c) transverse T8510 (3.5% CW), (d) transverse T8510 (4.5% CW), (e) longitudinal T3510 (3.5% CM), (f) longitudinal T3510 (4.5% CW), (g) longitudinal T8510 (3.5% CW), (h) longitudinal T8510 (4.5% CW).

Table 11. Grain size of ShAPE extruded and as-received 2024 tubes with different heat treatment.

Section Orientation	Grain size in μm @ different temper				
	T3510 3.5% CW	T3510 4.5% CW	T8510 3.5% CW	T8510 4.5% CW	As-received T351
Transverse	19.9 ± 9.2	19.2 ± 9.5	26.6 ± 19.5	20.9 ± 11.1	69.9 ± 31.3
Longitudinal	26.0 ± 11.6	22.0 ± 10.2	32.9 ± 17.8	26.5 ± 12.2	123.9 ± 62.5

Low magnification SEM backscattered electron (BSE) images of T3510 and T8510 conditions were compared in Figure 28 to evaluate the distribution of secondary phases. Breakdown and uniform distribution of secondary phases are common phenomenon in ShAPE processing of Al alloys [49, 50]. No significant difference of second phase distribution is observed in Figure 28.

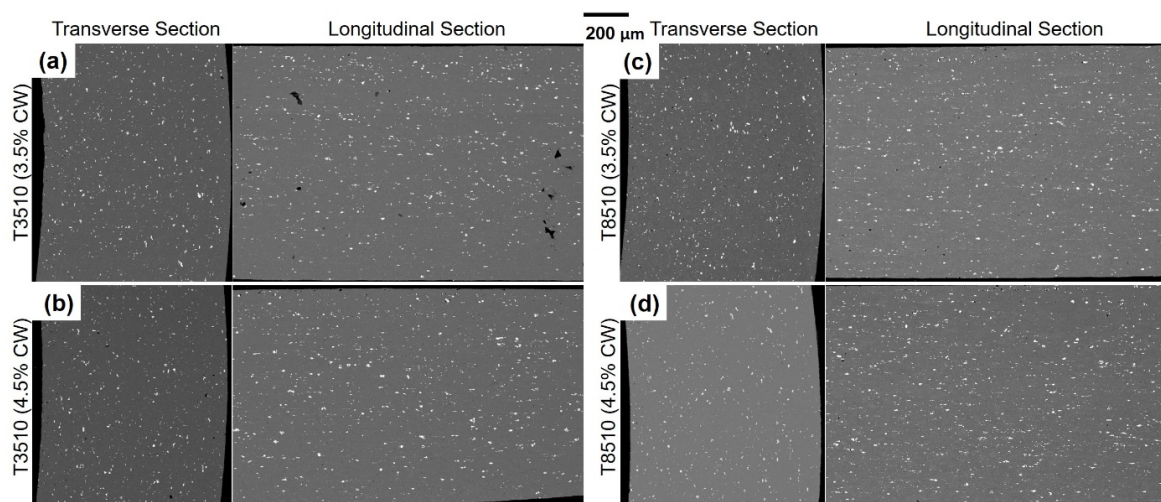


Figure 28. SEM images highlighting bright second phase precipitates in the transverse and longitudinal sections of 2024 ShAPE tubes after different post extrusion heat treatment: (a) T3510 (3.5% CW), (b) T3510 (4.5% CW), (c) T8510 (3.5% CW) and (d) T8510 (4.5% CW).

Therefore, a higher magnification SEM micrograph along with EDS elemental mapping in the middle of the transverse section are displayed in Figures 29(a-d) to further unveil the precipitate distribution. Previous literature has proven that the principal strengthening precipitates in age hardened 2024 system are S (Al_2CuMg) and Ω (Al_2Cu) phases [51, 52]. As SEM and EDS mapping in Figures 29(a-d) show, sparse and coarsened S phases ($\sim 1\text{-}5\ \mu\text{m}$) are observed in all four tempered conditions. In addition, a complicated secondary phase of AlCuFeMnSi ($\sim 5\text{-}30\ \mu\text{m}$) was also evident. The crack within the larger AlCuFeMnSi particle displayed in Figure 29(a) is a common phenomenon in these type of brittle intermetallic phases [53]. Note that the small bright spots in Figures 29(a-d) represent the nano sized precipitates, and that the amount of nano sized precipitates in T8510 (4.5% CW) condition displayed in Figure 29(d) is evidently less than the other three conditions displayed in Figures 29(a-c). This phenomenon is almost prevalent throughout the transverse and longitudinal sections in which relatively higher density and larger S phase was observed in the case of naturally aged (T3510) condition with 3.5-4.5% cold working (see Figure 29(a) and (b)). The cluster of S phase is also prominent in artificially aged T8510 with 3.5% CW (Figure 29(c)). However, the dispersion of S phase occurred gradually during the artificial aging (T8510) of 2024 after 4.5% cold working.

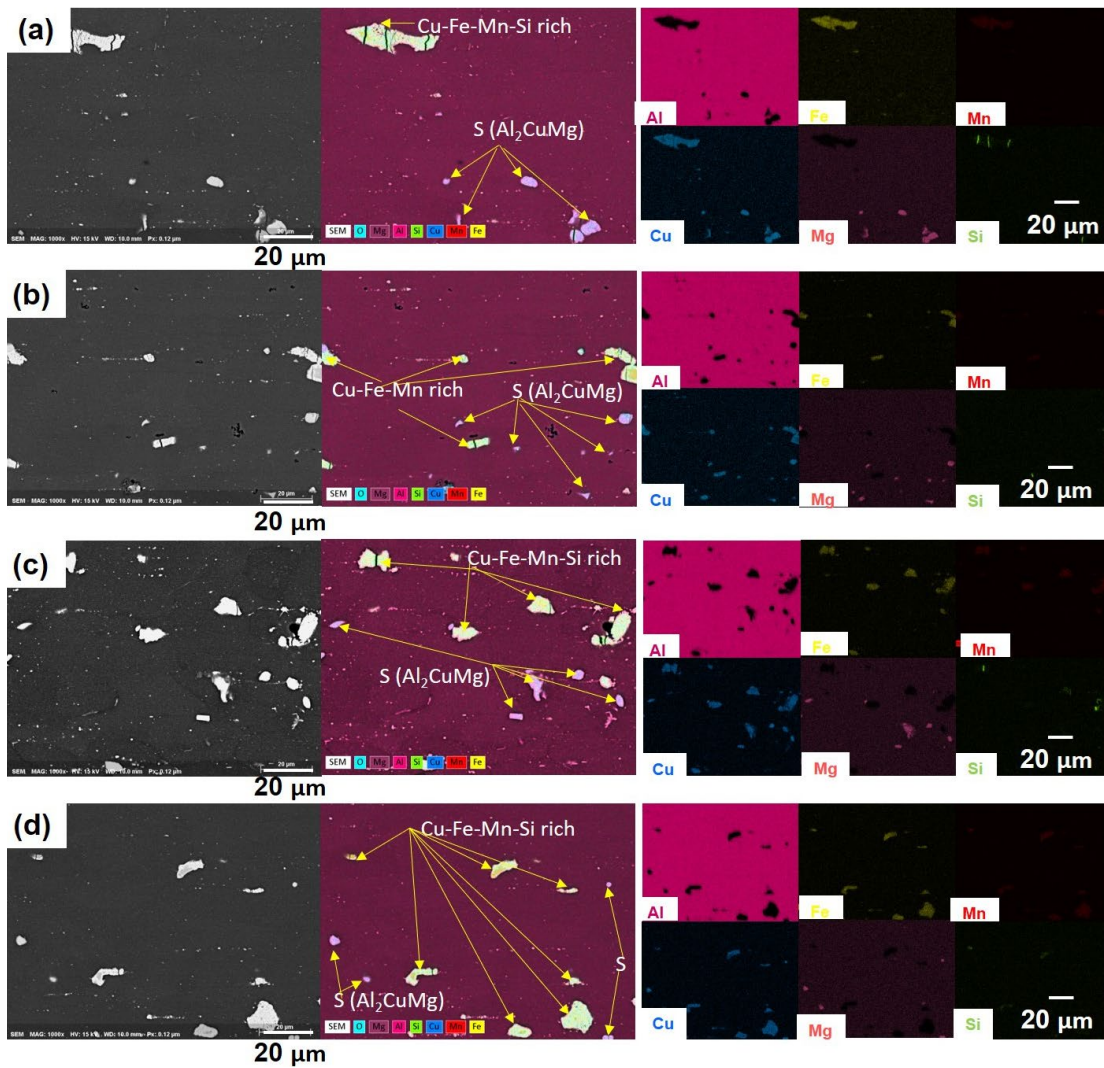


Figure 29. SEM EDS mapping illustrating the S phase in longitudinal sections of 2024 ShAPE tubes after different post extrusion heat treatment: (a) T3510 (3.5% CW), (b) T3510 (4.5% CW), (c) T8510 (3.5% CW) and (d) T8510 (4.5% CW).

Furthermore, higher resolution SEM images with EDS mapping in Figure 30 demonstrates the difference in the S phase distribution in 2024 tubes with T3510- 3.5 % CW (Figure 30(a)) and T8510- 4.5% CW (Figure 30(b)). The concentration of Mg in Figure 30(a) indicates S phase is localized in this area for T3510-3.5% CW condition. On the other hand, EDS mapping for the T8510-4.5% CW condition reveals that the Cu concentrates on bright areas while Mg distributes uniformly in the Al matrix which indicates that S phase further dissolves into the Al matrix during artificial aging. In addition, the randomly distributed Mn element in both conditions (Figure 30(a) and (b)) corresponds to T phase ($\text{Al}_{20}\text{Cu}_2\text{Mn}_3$) dispersoids in the Al matrix which was not detected previously in Figure 29 due to the nature of its small sizes. Although the S phase and Ω phase dissolve into the matrix at the SHT temperature, T phase precipitated during the SHT process and remains thermally stable during subsequent artificial aging which improves mechanical strength [53-55].

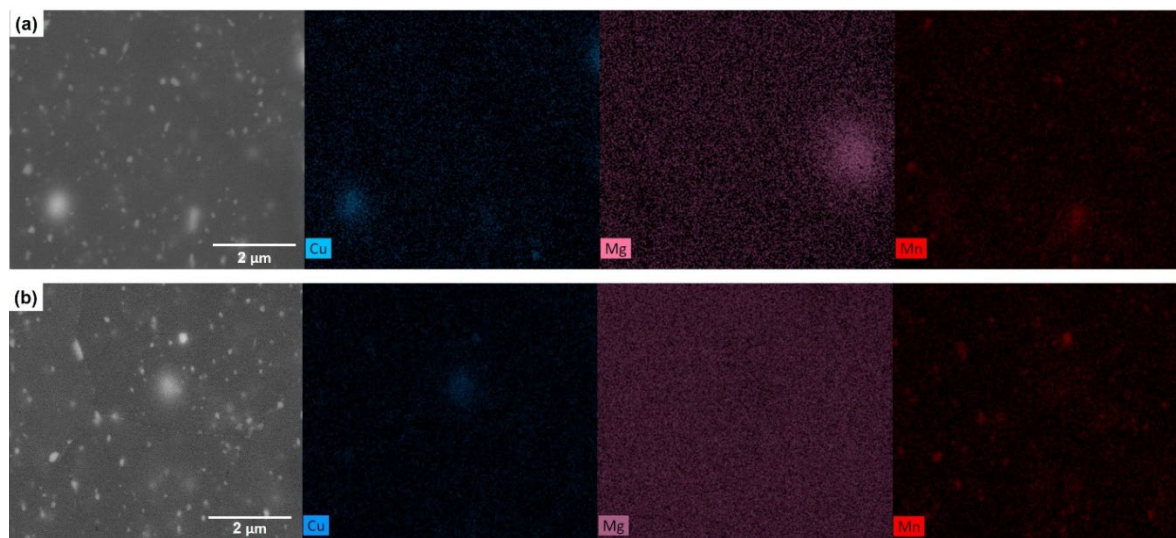


Figure 30. High resolution SEM BSE images with Cu, Mg and Mn mapping for 2024 tubes with (a) T3510-3.5% cold working and (b) T8510-4.5% cold working.

The ShAPE process enables the breakdown of secondary phases and dispersoids into finer sizes as well as a more homogeneous distribution of these fine particles, which favors enhancement of mechanical properties in the subsequent cold work and aging steps. This demonstrates one mechanism whereby ShAPE can achieve superior mechanical properties as compared with conventional extrusion methods. Note that for either ShAPE-T3510 or ShAPE-T8510 condition, strength increased with CW value increasing (Figures 25(a) and (b)). This is because increased CW results in a denser dislocation density around the T phase during CW process, and therefore more precipitate formation sites during subsequent aging.

Furthermore, the main strengthening precipitates vary between T3510 and T8510 conditions. For T3510, the main strengthening precipitates are Cu-Mg clusters (GPB zones) which formed during the final natural aging step. As for T8510, the main strengthening precipitates are S' and S phases which formed during the artificial aging step. In this study, S' and S phases in T8510 condition are more effective in strengthening the alloy but reduce the ductility as compared with the Cu-Mg clusters in T3510 condition. Moreover, dispersion of Mg atoms with higher aging time indicated the dissolution of S phase in matrix of 2024-T8510 (4.5% CW) that can initiate the lattice distortion during tensile testing of ShAPE extruded tubes. These solute atoms might also be responsible for improved yield strength of ShAPE extruded 2024-T8510 (4.5% CW) tube by impeding the dislocation motion.

ShAPE technology has successfully demonstrated extruding 12 mm diameter and 1 mm thick walled 2024 tubes at an extrusion speed of 7.4 m/min. With regard to mechanical properties, remarkable improvements in strength were achieved, in particular yield strength, without a proportional reduction in elongation at break compared to ASTM, ASM and industry values. The key observations and conclusions from the work on 2024 billets are as follows.

- The average UTS of ShAPE extruded 2024 tube is about 18-22% higher than the ASM typical and ASTM minimum values and about 2-8% higher than the maximum industry value for corresponding T3510 and T8510 heat treatment.
- The average 0.2% YS of ShAPE extruded 2024 tube is about 28-38% higher than the ASM typical and ASTM minimum values and about 10-24% higher than maximum industry values for corresponding T3510 and T8510 heat treatment.
- The ductility of ShAPE extruded 2024 tubes are double that of the ASM-typical and ASTM-minimum values and on the par of industry reported maximum values.
- ShAPE produced equiaxed grain structure in the longitudinal and transverse directions while also reducing the grain size of the precursor materials by 55-82%.
- Increased dispersion and uniform distribution of strengthening precipitates at sub-micron scale resulted in a higher YS in the ShAPE products.

4.5 ShAPE Extrusion of Al-12.4TM Powder

4.5.1 Mechanical Testing

Previous work on ShAPE of Al-12.4TM powder to manufacture 5 mm and 25.4 mm diameter rods showed that it was possible to forego the multiple steps involved in manufacturing components using powder metallurgy methodology from particulate feedstock. As such, it was hypothesized in this project that there were ShAPE process parameter windows for which it was possible to manufacture tubes from powder precursors in one-step approach. To that end, ShAPE was used to manufacture tubes in this project. Figure 31 shows the process conditions used to manufacture the Al-12.4TM tubes using ShAPE along with the corresponding extrusion forces, torque and temperature observed during extrusion. It is evident that the force and torque increased with increasing feed rate. In fact, when the die feed rate increased from 20 mm/min to 60 mm/min, the extrusion force increased by 50% from 170 kN to 255 kN. Correspondingly, the torque increased from 890 Nm to 1088 Nm by 22%. It is probably because that the amount of material to be processed in the same amount of time was increased. Also, a higher extrusion speed led to a lower processing temperature. With feed rate increasing from 20 mm/min to 60 mm/min and die rotational speed remaining unchanged, the steady-state extrusion temperature reduced from 610 °C to 570 °C owing to more heat and mass being taken away from the processing region over the same elapsed time.

Trial (#)	Ram Speed (mm/min)	Extrusion Ratio	Extrusion Speed (m/min)	Rotation Speed (rpm)
1	8	20.6	0.2	42
2	15	20.6	0.3	48
3	20	20.6	0.4	48
4	30	20.6	0.6	48
5	45	20.6	0.9	45
6	60	20.6	1.2	48

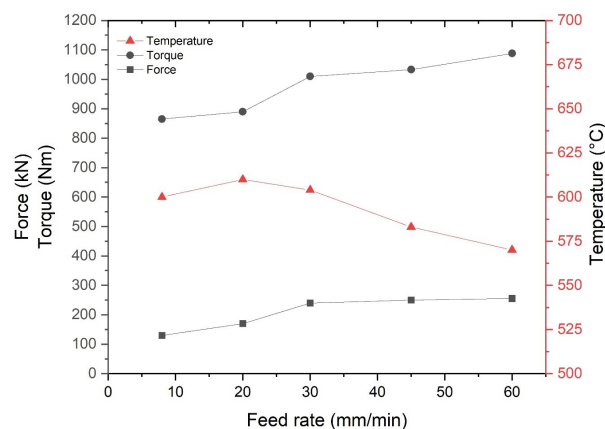


Figure 31. ShAPE process parameters used for manufacturing Al-12.4TM tubes in one-step approach and the corresponding extrusion forces, torque and temperatures observed during manufacturing.

The surface appearance of the tubes made with different feed rates is presented in Figure 32. At low feed rates (≤ 20 mm/min), scrolled undulation patterns can be seen clearly on the surfaces of the tubes. They are hypothesized to be formed due to eccentric rotation when the extrudates are long and the die advanced per revolution is low. With a similar die rotational speed and an increased feed rate, the undulation pitch increased while the tube also became straighter as seen in Figure 32. At feed rates of 45 mm/min and 60 mm/min, the undulation diminished, and the surface of the tubes was much smoother, although fine surface markings were still present.

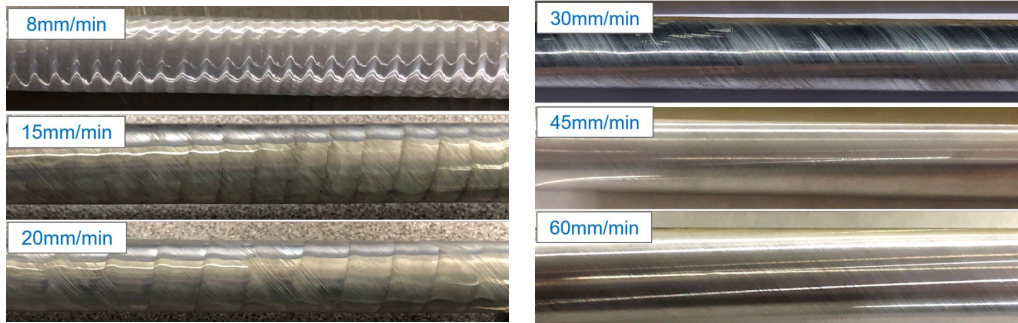


Figure 32. Surface features on the Al-12.4TM ShAPE tubes manufactured at an extrusion ratio of 20.6 and feed rates varying from 8 – 60 mm/min.

The average density of the ShAPE tubes was calculated from samples made by different feed rates and is presented in Figure 33(a) and compared with the density of the sintered sample and hot extruded samples available in literature [56]. The void free ShAPE samples demonstrate a higher density of 2.94 g/cm³ than the hot extrusion samples with a density of 2.91-2.93 g/cm³. The lowest density of 2.69 g/cm³ was observed for the sintered samples. The average Vicker’s hardness of ShAPE tubes made at different die feed rates are presented in Figure 33(b). The error bars represent the standard deviation in the measurements. The overall trend indicates that the average hardness decreased when the feed rate increased. Interestingly, the hardness of the outer diameter (OD) was consistently higher than that of the inner diameter (ID). The OD hardness increased with an increase in feed rate while the ID hardness decreased. As a result, the deviation of hardness through the tube wall thickness increased with an increased feed rate.

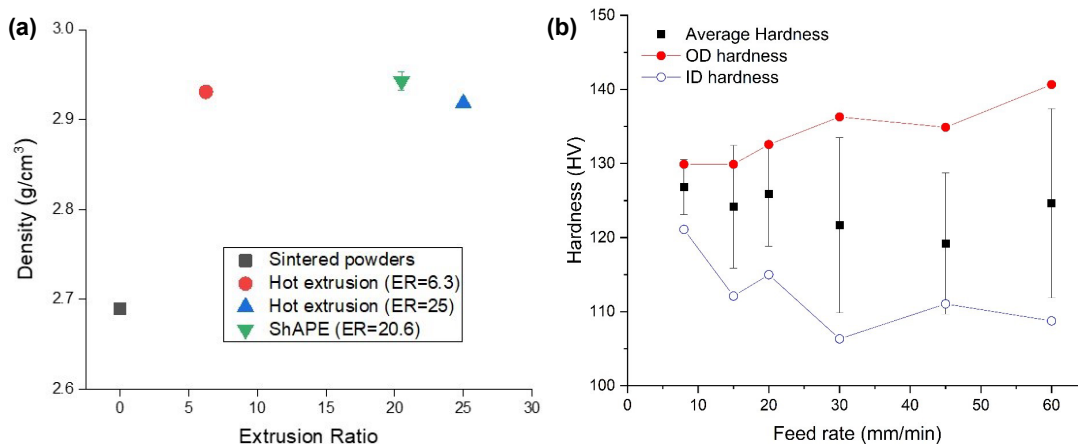


Figure 33. Density (A) and Vickers hardness (B) of Al-12.4TM ShAPE tubes products made with different feed rates.

4.5.2 Microstructural Characterization

An optical overview image of half of the longitudinal cross-section of the remnant precursor and the last part of the extruded tube manufactured at a rotation rate of 42 rpm and a feed rate

of 8 mm/min is presented at the top of Figure 34. The trend of macro and microstructure reveals the process of combined consolidation and extrusion in the SHAPE process.

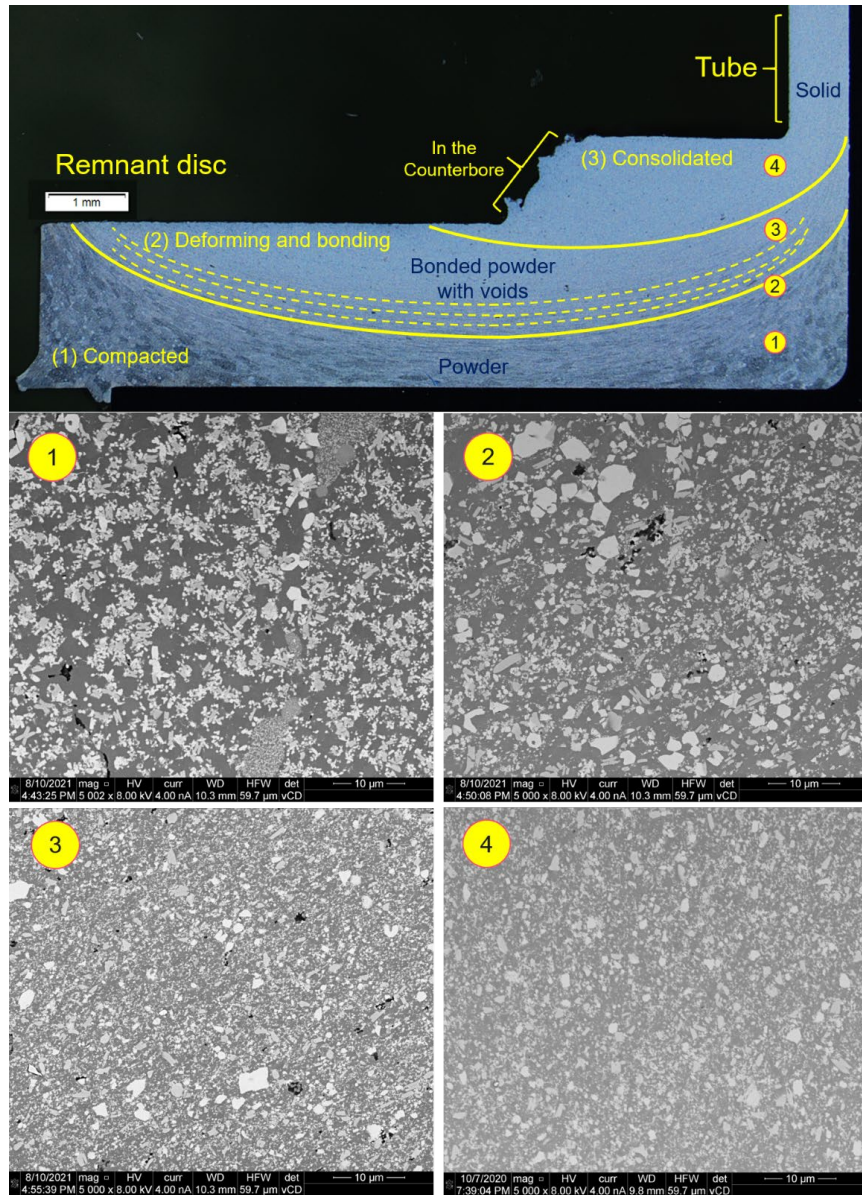


Figure 34. Top, An optical overview image of half of the longitudinal cross-section of the remnant precursor and the last part of the extruded tube, 42 rpm, 8 mm/min. Bottom, high magnification SEM images at locations 1-4 on the overview image.

Based on the degree of consolidation, the remnant material is divided into three regions from the bottom to the top:

- Zone (1) is the compacted zone at the bottom where the powder was only compressed by pressing but not shear-deformed. SEM image at location ① shows the size and shape of the second phase particles remained undeformed, and voids existed in this region.

- Zone (2) is the deforming and bonding zone. In this region, layered arc-like shear bands were formed horizontally and highlighted with dash lines in figure 34. These shear-induced structures were also observed in the remnant discs from other ShAPE and FE processes. At location ②, the boundary of the zone (1) and (2), the intermetallics are disturbed and sheared along with the bands. It indicates the onsite shear deformation and the orientation of the material flow. At location ③, the upper region of zone (2), the thickness of the material flow band was reduced while the voids were fragmented and closed compared to location ① and ②. The size of the reinforcing particles was highly refined from ~10 μm to submicron while their shape was ground from irregular to equiaxial due to internal attrition. The above observations manifest that material was strongly shear-deformed and bonded at an elevated temperature in this region.
- Zone (3) is the consolidated zone, which has nearly the same microstructure as the extruded tube. In the counterbore of the die, the material was further processed and fully consolidated into an integrated solid before extrusion. In the SEM image at location ④, the particles that were not broken in the deforming zone were fully refined and uniformly dispersed in the aluminum matrix. Voids were not observed in this region, which shows that the powder-to-bulk consolidation was achieved. The density results also support this conclusion.

In powder metallurgical processing, components are extruded after consolidating them. Consolidation is to convert loose discrete powders or particles into a solid material. Extrusion forms the consolidated green billet into the final product with the desired form factor. Conventionally, these are two separate processes with independent thermomechanical pathways. Also, each step requires its own equipment.

On the other hand, during the ShAPE process, the rotating die advances into the feedstock powder to simultaneously compact and plasticize it. The combination of friction between the tool face and the billet as well as the mechanical forces applied, deform and plasticize the powder feedstock while generating heat that increases the temperature and softens the billet. The voids between discrete particles are eliminated under high pressure, elevated temperatures, and severe shear plastic deformation. Consequently, the material is consolidated into an integrated solid at the deformation zone adjacent to the die face. Second phases are refined into smaller particle sizes at this stage and redistributed homogeneously in the deforming material. Then, under a proper die feed rate, the consolidated material is extruded through the gap between die orifice and mandrel to form a continuous long tube. If the feed rate is too high, the powder exits through the extrusion hole without being fully consolidated. Therefore, it forms a tube with poor strength or fails to form a solid tube. If the feed rate is too low, the temperature can be high enough to melt the aluminum substrate which precludes the formation of a solid tube by clogging the die exit hole.

Microstructure at the outer diameter and inner diameter of the ShAPE tubes made with 8 mm/min and 45 mm/min were investigated by SEM to understand the wide variation in hardness. Back scattered SEM images are presented in Figure 35 with inset images at a higher magnification. In the pictures, gray regions are the aluminum matrix, and bright particles are the reinforcing transition metal intermetallics.

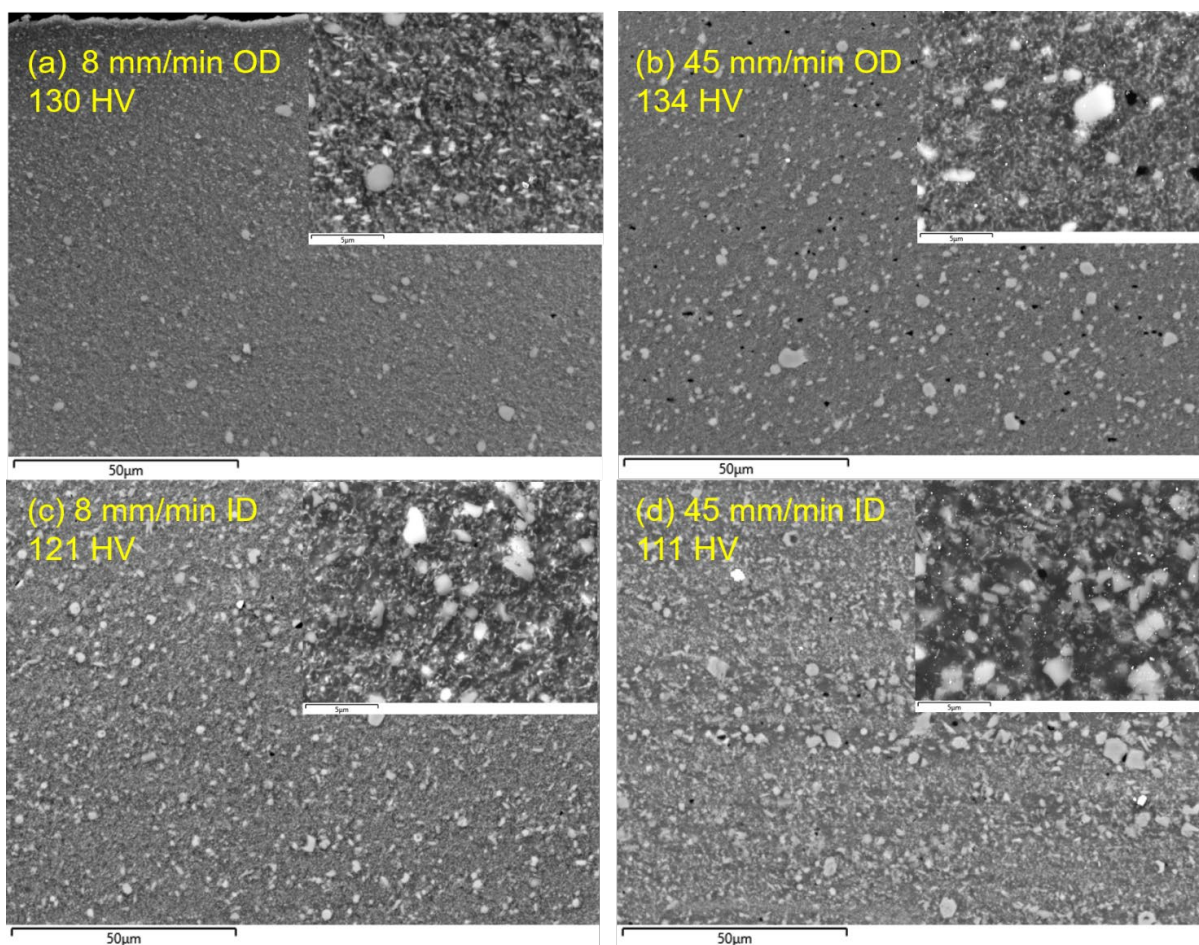


Figure 35. SEM of the ShAPE tubes made with different feed rates. (a) 8 mm/min, outer diameter; (b) 8 mm/min, inner diameter; (c) 45 mm/min, outer diameter; (d) 45 mm/min, inner diameter. Labelled with average Vicker's hardness. Inserts are higher magnification images with the length scale representing 5 μm.

Comparing the results at the outer diameter (OD) with inner diameter (ID), a comparatively higher density of macroscale second phase particles is observed for both samples along with the ID, in contrast to the OD tube wall. When correlated to hardness, the increased fraction of microscale intermetallics does not contribute to a strength increase. Instead, lower hardness is observed at the ID locations, where the effects of comparatively reduced shear are visible (insufficient shearing of second phase particles). At high magnification, increased shear encountered at the lower speed appears to have resulted in more significant second phase refinement at the OD. The higher number density of sub-micron second phases present along the OD of the 8 mm/min sample is likely responsible for increased hardness compared to the tube ID. This result agrees with hardness variation along the tube wall, where the shear gradient from the ID to the OD in both samples resulted in a visible intermetallics size gradient. Comparing 8 mm/min (Figures. 35(a), (c)) with 45 mm/min (Figures. 35(b), (d)), lower processing speed further refined the microstructure which contained higher density of sub-micron size intermetallics (<1 μm) and lesser number of voids across the wall thickness. This result is correlated to the reduced amount of applied shear per unit length when the feed rate increased, and rotation rate remained relatively the same. This lower density of submicron second phases in the 45 mm/min tube ID is likely responsible for the decreased hardness compared to the OD of the tube and the 8 mm/min tube.

The key findings from the Al-12.4TM powder-to-tube ShAPE study are as follows:

- ShAPE is capable of manufacturing tubes from powder feedstock in a single step without the need for compaction, sintering and other intermediary processes employed in powder metallurgy approaches.
- During ShAPE, the powder feedstock goes through compaction, consolidation, deformation, metallurgical bonding and extrusion sequentially.
- Higher extrusion feed rates reduce processing temperature and result in smoother tube surfaces compared to lower extrusion feed rates.
- Density of the ShAPE extrudates is higher than those manufactured by hot extrusion and are comparable or higher extrusion ratio demonstrating the effectiveness of the simultaneous application of normal and shear forces in densifying powder feedstock.
- Higher extrusion feed rates result in higher hardness along the tube outer wall and correspondingly lower hardness at the inner tube wall. The difference in hardness is inversely correlated to the density of the intermetallics present at measurement locations. This indicates that higher second phase deformation, fracture and distribution leading to sub-micron particles may lead to higher hardness in the ShAPE tubes.

5.0 Benefits Assessment

A techno-economic and energy analysis comparing ShAPE of 7075 with conventional extrusion was performed by NREL and is documented in a separate report [1]. The reader is referred to this extensive report which quantifies the reduced manufacturing energy and cost associated with ShAPE extrusion of 7075 compared to conventional extrusion.

6.0 Publications

The following articles have published and submitted for publication which cover the most impactful discoveries made on this project. The publication status is current as of the writing of this report.

- Steve Sikirica, S. Whalen, P. Kurup, H. Schwartz, H. Liddell, “Low-Energy, High-Throughput Extrusion of High-Strength Aluminum Alloy 7075,” *Industrial Heating*, April 2021, Cover Article. Status: Published
- Scott Whalen, M. Olszta, Md. Reza-E-Rabby, T. Roosendaal, T. Wang, D. Herling, B.S. Taysom, S. Suffield, N. Overman, “High Speed Manufacturing of Aluminum Alloy 7075 Tubing by Shear Assisted Processing and Extrusion (ShAPE),” *Journal of Manufacturing Processes*, 71, pp. 699-710. Status: Published
- Tianhao Wang, J. Atehortua, M. Song, Md. Reza-E-Rabby, B.S. Taysom, J. Silverstein, T. Roosendaal, D. Herling, S. Whalen, “Extrusion of Unhomogenized Castings of 7075 Aluminum,” *Materials and Design*, 213, 110374, 2022. Status: Published
- Md. Reza-E-Rabby, T. Wang, N. Canfield, T. Roosendaal, B.S. Taysom, D. Graff, D. Herling, S. Whalen, “Effect of Post-Extrusion Heat Treatment on Performance of AA2024 Tubes Fabricated by Shear Assisted Processing and Extrusion,” *CIRP Journal of Manufacturing Science and Technology*. Status: Accepted
- Xiao Li, T. Wang, X. Ma, N. Overman, S. Whalen, D. Herling, K. Kappagantula, “Manufacture of High-Temperature Aluminum Alloy Tube from Powder with a Single-Step Extrusion,” *Journal of Manufacturing Processes*. Status: Submitted

The following conference papers have been published and submitted. The publication status is current as of the writing of this report.

- Scott Whalen, Md. Reza-E-Rabby, T. Wang, X. Ma, T. Roosendaal, B.S. Taysom, “Shear Assisted Processing and Extrusion of Aluminum Alloy 7075 Tubing at High Speed,” *Light Metals*, 2021, pg. 277-280. Status: Published
- Md. Reza-E-Rabby, T. Wang, N. Canfield, D. Graff, T. Roosendaal, S. Whalen, “Effect of post extrusion heat treatment on mechanical property of aluminum alloy 2024 tube produced using Shear Assisted Processing and Extrusion (ShAPE),” *TMS*, 2022. Status: Submitted

7.0 Intellectual Property

Non-provisional patents filed:

- Scott Whalen, Md. Reza-E-Rabby, S. Taysom, D. Herling, G. Grant, V. Joshi, R. Kalsar, T. Wang, “Devices and Methods for Performing Shear-Assisted Extrusion and Extrusion Processes,” US Patent Application filed April 2021, PNNL Invention Disclosure: 31888
- Scott Whalen, J. Darsell, Md. Reza-E-Rabby, S. Taysom, T. Wang, D. Herling, X. Li, “Devices and Methods for Performing Shear-Assisted Extrusion and Extrusion Processes,” US Patent Application filed September 2021, PNNL Invention Disclosures: 31887, 32015, 32063

Provisional patents docketed for filing as non-provisional:

- Md. Reza-E-Rabby, S. Whalen, “High Strength Aluminum Alloy 2024 by Shear Assisted Processing and Extrusion,” Provisional Patent Application filed July 2021, PNNL Invention Disclosure: 32216
- Brandon Scott Taysom, Md. Reza-E-Rabby, S. Whalen, “Method of Quenching Immediately after ShAPE Extrusion,” Provisional Patent Application filed Sept 2021, PNNL Invention Disclosure: 31921

8.0 Awards and Recognition

This project was a key provider of technical accomplishments that contributed to the winning of three prestigious awards.

- R&D 100 Award in the Process/Prototyping Category, 2020
- Association of Washington Business Manufacturing Excellence Award in the Green Manufacturing Category, 2021
- PNNL Project of the Year in the Energy Processes and Materials Division, 2020
- Article in Industrial Heating Magazine was selected as cover art for April, 2020 issue

9.0 Concluding Remarks

ShAPE has been developed for high-performance aluminum alloys to extrude hollow profiles with improved material properties compared to ASTM standards, ASM values, and highest industry values for conventional extrusion. Simultaneously, ShAPE enabled a substantial increase in extrusion speed compared to conventional extrusion and eliminated energy intensive heat treatment steps such as billet homogenization, billet pre-heating, and post-extrusion solution heat treatment. Results from this project demonstrate that ShAPE has the potential to enable step-change improvements in material performance while reducing energy consumption, and in turn carbon emissions. Research performed on this project sets the stage for future work where lessons learned are leveraged into other aluminum alloys, aluminum recycling, exotic materials for extreme environments, industrial scalability, and evolution into extrusion of complex multi-cell profiles that are typical of conventional extrusion.

10.0 Recommendations

The ShAPE tooling and process parameters developed on this project should be leveraged into the following areas.

- **Aluminum-Cerium:** This alloy is promising for aerospace applications that require high strength and fatigue resistance at elevated temperature. However, traditional extrusion techniques do not adequately refine the blocky $Al_{11}Ce_3$ second phase. ShAPE offers the potential to greatly improve the strength, elongation, toughness, and fatigue resistance in Al-Ce when extruding directly from castings (akin to the 7075 castings in this work).
- **Recycling:** Hundreds of metric tons of 6XXX and 7XXX scrap is created every day in the automotive and aerospace industries. ShAPE can convert this scrap directly into semi-finished components with better material properties than the scrap started with, without re-melting or adding primary aluminum. Scrap from junkyards, such as window frames and gutters, can be shredded and converted directly into useful components as well. Development of ShAPE for recycling without re-melting, and without adding primary aluminum, is an opportunity to realize dramatic energy and carbon savings in the aluminum recycling industry. Titanium recycling is another opportunity since titanium scrap is nearly 100% recyclable but needs to be combined with approximately 50% fresh titanium sponge. Using ShAPE to convert titanium scrap directly into hydraulic tubing and bar stock for fasteners, without the need for titanium sponge or re-melting, would enable energy savings, lower cost components, and reduced dependence on other countries for the supply of titanium sponge.
- **Materials for Extreme Environments:** Oxide dispersion strengthened steels, intermetallics, and aluminides extruded by ShAPE offer the potential for even higher performing materials in the most demanding environments.

11.0 References

- [1] A. Sertac, C. Kinchin, P. Kurup, Techno-Economic Analysis for Shear Assisted Processing and Extrusion (ShAPE) of High Strength Aluminum Alloys, NREL/TP-7A40-80038 Technical Report, December 2021.
- [2] S. Whalen, N. Overman, V. Joshi, T. Varga, D. Graff, C. Lavender, Magnesium Alloy ZK60 Tubing made by Shear Assisted Processing and Extrusion (ShAPE), Materials Science and Engineering A, 755 (7), 278-288, 2019.
- [3] J. Croteau, J. Jung, S. Whalen, J. Darsell, A. Mello, D. Holstine, K. Lay, M. Hansen, D. Dunand, N. Vo, Ultra-Fine Grained Al-Zr Processed by Shear Assisted Processing and Extrusion with High Thermal Stability, Scripta Materialia, vol. 186, pp. 326-330, 2020.
- [4] Sheppard T, Extrusion of Aluminum Alloys, Springer Science & Business Media Dordrecht, 1999, pg. 239.
- [5] Canadian Aeronautics and Space Journal, vol. 35-36, 1989, pg. 129.
- [6] 2024-T351 Wrought Aluminum Alloy Technical Data Sheet, Alcoa Corporation.
- [7] Lavender C, Joshi V, Grant G, Jana S, Whalen S, Darsell J, Overman N, System and Process for Formation of Extrusion Products, US 10189063, 2019.
- [8] Aluminum Extrusion Market: Global Industry Trends, Share, Size, Growth, Opportunity and Forecast 2021-2026." IMARC 2021. <https://www.imarcgroup.com/aluminium-extrusion-market>.
- [9] Scott Whalen, Md. Reza-E-Rabby, S. Taysom, D. Herling, G. Grant, V. Joshi, R. Kalsar, T. Wang, Devices and Methods for Performing Shear-Assisted Extrusion and Extrusion Processes, US Patent Application filed April 2021, PNNL Invention Disclosure: 31888
- [10] Scott Whalen, J. Darsell, Md. Reza-E-Rabby, S. Taysom, T. Wang, D. Herling, X. Li, Devices and Methods for Performing Shear-Assisted Extrusion and Extrusion Processes, US Patent Application filed September 2021, PNNL Invention Disclosures: 31887, 32015, 32063
- [11] Md. Reza-E-Rabby, S. Whalen, High Strength Aluminum Alloy 2024 by Shear Assisted Processing and Extrusion, Provisional Patent Application filed July 2021, PNNL Invention Disclosure: 32216
- [12] Scott Whalen, J. Darsell, Md. Reza-E-Rabby, S. Taysom, T. Wang, D. Herling, X. Li, Devices and Methods for Performing Shear-Assisted Extrusion and Extrusion Processes, US Patent Application filed September 2021, PNNL Invention Disclosures: 31887, 32015, 32063
- [13] Hilditch T, de Souza T, Hodgson P, Properties and Automotive Applications of Advanced High Strength Steels (AHSS), Welding and Joining of Advanced High Strength Steels (AHSS), edited by Shome M and Tumuluru M, Woodhead Publishing, 2015, pg. 9-28.
- [14] Joost W, Reducing Vehicle Weight and Improving U.S. Energy Efficiency Using Integrated Computational Materials Engineering, JOM, vol. 64, 2012, pg. 1032-1038.

- [15] United States Environmental Protection Agency, Greenhouse Gas Emissions from a Typical Passenger Vehicle, Office of Transportation and Air Quality, EPA-420F-18-008, 2018.
- [16] Hashimoto N, Application of Aluminum Extrusions to Automotive Part, Kobelco Technology Review, vol. 35, 2017, pg. 69-75.
- [17] 6061 Aluminum vs 7075 Aluminum. Parts Badger. 2019. <http://parts-badger.com/6061-vs-7075-aluminum/>.
- [18] Aluminum Extrusion Technology, edited by Saha P, ASM International, 2000, pg. 190.
- [19] ASM Handbook Volume 14A: Extrusion of Aluminum Alloys, edited by Misiolek W, Kelly R, ASM International, 2005, pg. 523.
- [20] Sheppard T, Extrusion of Aluminum Alloys, Springer Science & Business Media Dordrecht, 1999, pg. 82.
- [21] Suh D, Lee S, Lee K, Lim S, Oh K, Microstructural Evolution of Al-Zn-Mg-Cu-(Sc) Alloy During Hot Extrusion and Heat Treatments, J Mater Process Technol, Vol. 155-156, 2004, pg. 1330-1336.
- [22] Zakharov V, Scientific Aspects of Deformability of Aluminum Alloy During Extrusion, Adv Perform Mater, vol. 2, 1995, pg. 51-66.
- [23] S. Whalen, M. Olszta, C. Roach, J. Darsell, D. Graff, Md. Reza-E-Rabby, T. Roosendaal, W. Daye, T. Pelletiers, S. Mathaudhu, N. Overman, High Ductility Aluminum Alloy made from Powder by Friction Extrusion, Materialia, 6, 100260, 2019.
- [24] J. Pickens, High Strength Aluminum P/M Alloys, in ASM Metals Handbook. 1990. p. 200-215.
- [25] R.W. Stevenson, P/M Lightweight Metals, in ASM Metals Handbook. 1984, American Society for Metals: Metals Park, OH. pg. 741-764.
- [26] W. Jones, Fundamental Principles of Powder Metallurgy, Edward Arnold, London (1960). Google Scholar: p. 245-260.
- [27] M. Erinosh, E. Angula, F. Nangolo, B. Ikotun, O. Johnson, Technical Review on Severe Plastic Deformation of Aluminum Series, Advances in Material Science and Engineering, 2021, pg. 55-83.
- [28] W. Poole, M. Wells, D. Lloyd, Processing of Aluminum Alloys by Severe Plastic Deformation, Materials Science Forum, vol. 519-521, 45-54, 2006
- [29] S. Behera, S. Chadaram, M. Banda, A Review of Severe Plastic Deformation, International Journal of Advanced Materials Manufacturing and Characterization, 3(1), pg. 291-295, 2013.
- [30] A. Fadhi, Spiral Friction Stir Processing (SFSP) for the Extrusion of Lightweight Alloy Tubes, Proceedings of the ASME 2012 International Manufacturing Science and Engineering Conference, Notre Dame, Indiana, MSEC2012-7358.

- [31] A. Fadhi, A Preliminary Study on the Feasibility of Friction Stir Back Extrusion Materialia, 66, 2012, pg. 615-618.
- [32] S. Zhang, A. Frederick, Y. Wang, M. Eller, P. McGinn, A. Hu, Z. Feng, Microstructure Evolution and Mechanical Property Characterization of 6063 Aluminum Alloy Tubes Processed with Friction Stir Back Extrusion, JOM, 71(12), 2019, pg. 4436-4444.
- [33] J. Milner, A. Fadhi, Microstructural Evolution and its Relationship to the Mechanical Properties of Mg AZ31B Friction Stir Back Extrusions, 2014, pg. 263-268.
- [34] W. Daye, T. Pelletiers, W. Thomas, Property Development of New Generation PM Aluminum Materials via Innovative Processing, International Journal of Powder Metallurgy, 54(2), 2018.
- [35] ASTM B557-15, Standard Test Methods for Tension Testing Wrought and Cast Aluminum and Magnesium Alloy Products.
- [36] ASTM B221-14, Standard Specification for Aluminum and Aluminum-Alloy Extruded Bars, Rods, Wires, Profiles, and Tubes, vol. 02.02, ASTM International.
- [37] ASM Handbook Volume 2b - Properties and Selection of Aluminum Alloys, 7075 and Alclad 7075, edited by Anderson K, Weritz J, Kaufman G, ASM International, 2019, pg. 432-438.
- [38] Manufacturing and Design, edited by Tempelman E, Shercliff H, Ninaber van Eyben B, Betterworth-Heinmann, 2014, pg. 71.
- [39] Extrusion: Process Machinery Tooling, edited by Laue K, Stenger H, American Society for Metals, 1981, pg. 126
- [40] Bauser M, Historic Development of Extrusion, Extrusion: Second Edition, edited by Bauser M, Sauer G, Siegert K, ASM International, 2006, pg. 2-8.
- [41] Mackenzie J, "Second Paper on Statistics Associated with the Random Disorientation of Cubes," Biometrika, vol. 45, iss. 1-2, 1958, pg. 229-240.
- [42] C. Genevois, A. Deschamps, A. Denquin, B. Doisneau-Cottignies, Quantitative investigation of precipitation and mechanical behaviour for AA2024 friction stir welds, Acta Materialia, 53 (2005) 2447-2458.
- [43] Z. Zhang, B. Xiao, Z. Ma, Hardness recovery mechanism in the heat-affected zone during long-term natural aging and its influence on the mechanical properties and fracture behavior of friction stir welded 2024Al-T351 joints, Acta materialia, 73 (2014) 227-239.
- [44] K. Anderson, J.G. Kaufman, J. Weritz, ASM Handbook: Volume 2B Properties and Selection of Aluminum Alloys, ASM International, 2019.
- [45] D.S. MacKenzie, Heat Treatment Practice of Wrought Age-Hardenable Aluminum Alloys, in: K.F. Anderson, J. Weritz, J.G.F. Kaufman (Eds.) Aluminum Science and Technology, ASM International, 2018, pp. 462-477.

- [46] ASTM B221-20, Standard Specification for Aluminum and Aluminum-Alloy Extruded Bars, Rods, Wire, Profiles, and Tubes, in, ASTM International, West Conshohocken, PA, 2020.
- [47] K. Aluminum, Tube and Pipe Alloy 2024 Technical Data Sheet, in, 2006.
- [48] A. Eivani, H. Jafarian, J. Zhou, Simulation of peripheral coarse grain structure during hot extrusion of AA7020 aluminum alloy, *Journal of Manufacturing Processes*, 57 (2020) 881-892.
- [49] S. Whalen, M. Reza-E-Rabby, T. Wang, X. Ma, T. Roosendaal, D. Herling, N. Overman, B.S. Taysom, Shear Assisted Processing and Extrusion of Aluminum Alloy 7075 Tubing at High Speed, in: *Light Metals 2021: 50th Anniversary Edition*, Springer International Publishing, 2021, pp. 277-280.
- [50] B.S. Taysom, S. Whalen, M. Reza-E-Rabby, T. Skrzek, M. DiCiano, Shear Assisted Processing and Extrusion of Thin-Walled AA6063 Tubing, in: *Light Metals 2021: 50th Anniversary Edition*, Springer International Publishing, 2021, pp. 281-285.
- [51] C. Genevois, A. Deschamps, A. Denquin, B. Doisneau-Cottignies, Quantitative investigation of precipitation and mechanical behaviour for AA2024 friction stir welds, *Acta Materialia*, 53 (2005) 2447-2458.
- [52] Y.L. Zhao, Z.Q. Yang, Z. Zhang, G. Su, X. Ma, Double-peak age strengthening of cold-worked 2024 aluminum alloy, *Acta Materialia*, 61 (2013) 1624-1638.
- [53] M. Liang, L. Chen, G. Zhao, Y. Guo, Effects of solution treatment on the microstructure and mechanical properties of naturally aged EN AW 2024 Al alloy sheet, *Journal of Alloys and Compounds*, 824 (2020) 153943.
- [54] Z. Feng, Y. Yang, B. Huang, M. Li, Y. Chen, J. Ru, Crystal substructures of the rotation-twinned T (Al₂₀Cu₂Mn₃) phase in 2024 aluminum alloy, *Journal of alloys and compounds*, 583 (2014) 445-451.
- [55] Z. Shen, C. Liu, Q. Ding, S. Wang, X. Wei, L. Chen, J. Li, Z. Zhang, The structure determination of Al₂₀Cu₂Mn₃ by near atomic resolution chemical mapping, *Journal of alloys and compounds*, 601 (2014) 25-30.
- [56] Daye, W.K., I. Pelletiers, and W. Thomas, Property development of new generation pm aluminum materials via innovative processing. *Int. J. Powder Metall*, 2018. 54(2): p. 35-51.

Pacific Northwest National Laboratory

902 Battelle Boulevard
P.O. Box 999
Richland, WA 99354
1-888-375-PNNL (7665)

www.pnnl.gov